J. Fluid Mech. (2003), *vol.* 483, *pp.* 165–197.
DOI: 10.1017/S0022112003004129 Printed in the United Kingdom

A model for diffusion-controlled solidification of ternary alloys in mushy layers†

By D. M. ANDERSON

Department of Mathematical Sciences, George Mason University, Fairfax, VA 22030, USA

(Received 30 July 2002 and in revised form 26 December 2002)

We describe a model for non-convecting diffusion-controlled solidification of a ternary (three-component) alloy cooled from below at a planar boundary. The modelling extends previous theory for binary alloy solidification by including a conservation equation for the additional solute component and coupling the conservation equations for heat and species to equilibrium relations from the ternary phase diagram. We focus on growth conditions under which the solidification path (liquid line of descent) through the ternary phase diagram gives rise to two distinct mushy layers. A primary mushy layer, which corresponds to solidification along a liquidus surface in the ternary phase diagram, forms above a secondary (or cotectic) mushy layer, which corresponds to solidification along a cotectic line in the ternary phase diagram. These two mushy layers are bounded above by a liquid layer and below by a eutectic solid layer. We obtain a one-dimensional similarity solution and investigate numerically the role of the control parameters in the growth characteristics. In the special case of zero solute diffusion and zero latent heat an analytical solution can be obtained. We compare our predictions with previous experimental results and with theoretical results from a related model based on global conservation laws described in the Appendix. Finally, we discuss the potentially rich convective behaviour anticipated for other growth conditions.

1. Introduction

The solidification of multicomponent alloys is a central part of many industrial processes and natural phenomena. Often alloy solidification is accompanied by the formation of a mushy layer, which is a porous region made up of dendritic crystals surrounded by the residual melt. This mushy region separates the region occupied by the completely solidified material from that occupied by the melt phase. The presence of a mushy layer during solidification can greatly influence the transport of heat, mass and solute in these systems, and therefore the final solidified product. Observation and measurement of mushy layer dynamics in industrial and geophysical environments may be difficult, costly, dangerous or impossible. Consequently, laboratory experiments and theoretical models play critical roles in the understanding of alloy solidification in mushy layers.

There has been considerable progress over the last few decades in the understanding of binary alloy solidification in mushy layers, owing to theoretical modelling and experimental research. Introductions to this subject as well as literature reviews can be found in Davis (2001) and Worster (1997, 2000).

† With an Appendix by A. F. Thompson, H. E. Huppert & M. G. Worster.

In the present paper we are interested in studying the solidification of a ternary alloy and the accompanying mushy layer formation. The general motivation for this work lies in the wide variety of applications that involve the solidification of multicomponent alloys. More specifically, the present work has been inspired by experiments on a ternary alloy performed by Aitta, Huppert & Worster (2001*a*, *b*).

They investigated solidification of the ternary alloy H_2O–KNO_3–$NaNO_3$ from a cooled boundary. The operating regime for their experiments was such that the growth was diffusion-controlled; convection, including that due to thermal and solutal buoyancy, was absent. Their experiments showed that during ternary alloy solidification two distinguishable mushy layers can form between a liquid layer above and a eutectic solid layer below. The ternary phase diagram for this system provided the key to how these mushy layers could be distinguished: each mushy layer could be related to a different region of the ternary phase diagram (see below for further details). Their experimental measurements included data for the positions of the three interfaces separating the four layers (liquid layer, primary mushy layer, secondary mushy layer, and the eutectic solid layer). They found that after an early time regime in which disequilibrium effects dominated, the interface data could be fitted by a $t^{1/2}$ power law suggesting diffusion-controlled growth.

With these experiments in mind, we develop here a diffusion-controlled model for one-dimensional solidification of a ternary alloy that includes mushy layer formation. Our model extends in a natural way the diffusion-controlled model for one-dimensional solidification of a binary alloy derived and studied by Worster (1986). The mushy layer in that system, which developed owing to constitutional supercooling of the liquid ahead of a solidification front, was modelled as a separate phase from the solid and liquid layers. Thermal and solutal conservation laws were formulated in the mushy layer on a macroscale assumed to be much larger than the typical scale of the dendritic pore size in the mushy layer. The solid volume fraction was treated as a dependent variable which varied in space and time and was determined by invoking a thermodynamic equilibrium argument in the mushy layer. Results in the form of a similarity solution gave predictions for temperature and solute profiles through the system, the solid fraction profile in the mushy layer and the growth characteristics of the interfaces separating the liquid, mushy and solid layers.

Models that extend that of Worster (1986) and still admit a similarity solution have been studied. Chiareli & Worster (1992) developed a model accounting for expansion or contraction flow due to density change upon solidification. Voller (1997) addressed the case of partial solute rejection and a more general solute model which included the Scheil equation limit (zero solid-state diffusion), the lever rule limit (complete solid-state diffusion) and cases in between corresponding to finite back diffusion. The model of Voller could also be used in limited cases to address ternary alloy solidification. The limitations are constant segregation coefficients, zero solute diffusion and a linear relationship between the compositions and the temperature. These are conditions of interest in the present paper, although we shall set up our model to explicitly take into account the presence of two distinguishable mushy layers as observed in the experiments by Aitta *et al.*

There are several existing ternary alloy models incorporating mushy layers. One that bears a close resemblance to the present model is due to Krane, Incropera & Gaskell (1997). In their model, convection and diffusion were included in a ternary alloy mushy layer system that included both primary and secondary solidification scenarios as described above. In their model, the solidification boundaries were treated implicitly in a single computational domain. Their model is well suited to

two- or three-dimensional simulations of convective patterns and macrosegregation in ternary alloys, which they have performed for the ternary alloy Pb–Sb–Sn (Krane & Incropera 1997; Krane, Incropera & Gaskell 1998). Felicelli, Poirier & Heinrich (1997) formulated a model for the solidification of a multicomponent alloy which includes convective and diffusive transport associated with primary solidification. They computed convection and macrosegregation for selected ternary and quaternary alloys in two and three dimensions (Felicelli *et al.* 1997; Felicelli, Poirier & Heinrich 1998). Computations of micro- and macrosegregation in nickel-base superalloys and the associated mushy layer formation have been performed by Schneider *et al.* (1997) using a model by Schneider & Beckermann (1995) into which has been incorporated a phase equilibrium subroutine for nickel-base superalloys (Boettinger *et al.* 1995). This phase equilibrium subroutine, which provides realistic phase diagram data, has also been incorporated into computations of remelting of dendrite fragments of nickel-base superalloys (Gu, Beckermann & Giamei 1997). Our paper presents a detailed analysis of a ternary alloy mushy layer model related to those above but in which interfacial boundaries and associated interfacial conditions are treated explicitly and in which a ternary phase diagram reasonable for the experimental system of Aitta *et al.* is employed.

The paper is organized as follows. We first describe the ternary phase diagram used in the development and understanding of the model. We then formulate the one-dimensional solidification model including the governing equations and interfacial conditions. Next we express the model in terms of a similarity variable. We then give an analytical solution of this similarity system in the limit of vanishing solute diffusion and latent heat. Numerical solutions are then presented for the general case. We conclude with a discussion of possible convective scenarios for this ternary mushy layer system.

2. The ternary phase diagram

An essential part of the model and a key to understanding ternary alloy solidification is the ternary phase diagram, which identifies the equilibrium phase of a material at a given temperature and composition. Ternary phase diagrams for many real systems can be extremely complex (e.g. see Smallman 1985 or Boettinger *et al.* 1995). The one used in the simulations by Krane *et al.* (1997) includes, for example, intermetallic phases, a peritectic point and a eutectic point. We consider a highly simplified ternary phase diagram based on two key assumptions. The first is that no solid solutions form (complete solid immiscibility). The second assumption is that all liquidus surfaces and cotectic curves are linear (that is, there exists a linear relationship between the temperature and composition along these boundaries). These simplifications allow us to make the best use of the information on the phase diagram for the system H_2O–KNO_3–$NaNO_3$ provided by the experimental work of Aitta *et al.* (2001*a*) while at the same time keeping the description as simple as possible. We provide further details of these assumptions below.

A sketch of such a ternary phase diagram is shown in figure 1. We denote the liquid compositions of components A, B and C by A, B and C, where $A + B + C = 1$. The three corners of the ternary phase diagram correspond to the pure materials A, B and C and the vertical axis corresponds to temperature. Each of the three sides of the phase diagram corresponds to the binary phase diagram associated with two non-vanishing solute components. For example, the side connecting corner A with corner B represents the A–B binary eutectic phase diagram ($C = 0$ on this side). The melting

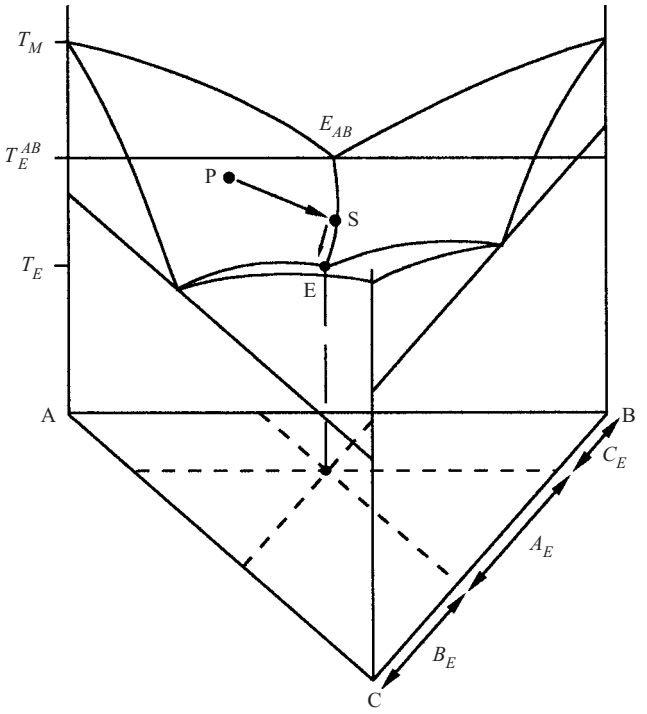

FIGURE 1. The ternary phase diagram used in the model.

temperature of pure A is T_M, the binary eutectic point (point E_{AB}) has temperature T_E^{AB} and composition of the B component B_E^{AB}. The binary liquidus curves along each of the three sides extend into the interior of the ternary phase diagram to form three liquidus surfaces. Along each side cotectic curves extend from the binary eutectic points into the interior of the phase diagram and are the boundaries of the liquidus surfaces. These three cotectic curves join together at the ternary eutectic point where the temperature is T_E and the compositions are A_E, B_E and C_E. The composition at any location in the phase diagram can be read from the triangle at the base as indicated for the example of the eutectic composition. A more detailed discussion of ternary phase diagrams is given by Smallman (1985).

The different phases that are present during the solidification of our ternary alloy may be mapped out by considering a solidification path, or liquid line of descent, through the phase diagram. Consider a liquid-phase ternary alloy that upon cooling reaches the point P on a liquidus surface. As the alloy is cooled further, solid A, composed of pure A, begins to solidify out while the components B and C are rejected into the liquid. The resulting increase of component B and C in the liquid corresponds to a solidification path which descends along the liquidus surface towards point S on the cotectic curve. The portion of the solidification path along the liquidus surface corresponds to the formation of the primary mushy layer made up of dendrites of solid phase A surrounded by residual liquid. Once the cotectic boundary is reached at point S solidification continues as both solid A (pure A) and solid B (pure B) form and the liquid compositions follow the cotectic curve in the direction of the ternary eutectic point. The portion of the solidification path along the cotectic curve corresponds to the formation of the secondary mushy layer made up of both solid A

and solid B crystals surrounded by the residual liquid. Once the eutectic point (point E) is reached, the remaining liquid solidifies to form a eutectic solid layer composed of solid A, solid B and solid C. Part of the solution to our model will be values for the solid volume fractions ϕ_A, ϕ_B and ϕ_C for the solid phases in the solid and mushy layers. With this brief description we return to our two key assumptions.

The assumption of complete immiscibility in the solid phases (see Smallman 1985) states that solid phase A is composed of pure A (no solute B or C is incorporated). Similarly, solid phase B is composed of pure B and solid phase C is composed of pure C.

Our second assumption is that the relation between temperature and composition along the liquidus surfaces and cotectic curves is linear. We may confine our attention to a single liquidus surface and a single cotectic line without loss of generality. We define the liquidus surface associated with the corner A and the cotectic line extending from the A–B side of the phase diagram in terms of the temperature and composition coordinates at the following three points: the melting point of pure A (where $B = C = 0$ and $T = T_M$), the binary eutectic point for the A–B system (where $B = B_E^{AB}$, $C = 0$ and $T = T_E^{AB}$) and the ternary eutectic point (where $B = B_E$, $C = C_E$ and $T = T_E$). The liquidus surface associated with corner A is most naturally defined in terms of the compositions B and C as

$$T^{\mathscr{L}}(B, C) = T_M + m_B B + m_C C, \tag{2.1}$$

where m_B and m_C are the constant liquidus slopes that relate changes in temperature to changes in composition B and C, respectively. Based on this definition we shall choose to work with components B and C noting that $A = 1 - B - C$. The cotectic line extending from the A–B side of the ternary phase diagram can be represented as

$$T = -m_B^{\mathscr{C}}(B - B_E) + T_E = -m_C^{\mathscr{C}} C + T_E^{AB}, \tag{2.2}$$

where $m_B^{\mathscr{C}}$ and $m_C^{\mathscr{C}}$ are constant slopes of the cotectic line that relate changes in temperature to changes in composition B and C, respectively. These liquidus and cotectic slopes can be expressed in terms of the above three coordinate points. We have

$$m_B^{\mathscr{C}} = \frac{T_E^{AB} - T_E}{B_E - B_E^{AB}}, \quad m_C^{\mathscr{C}} = \frac{T_E^{AB} - T_E}{C_E}, \tag{2.3}$$

$$m_B = -\frac{T_M - T_E^{AB}}{B_E^{AB}}, \quad \frac{m_B}{m_B^{\mathscr{C}}} + \frac{m_C}{m_C^{\mathscr{C}}} = -1, \tag{2.4}$$

where the last relation follows from noticing that the cotectic line is mathematically part of the liquidus surface. We can solve equations (2.2) and equivalently express the compositions B and C along the cotectic line as the linear functions defined by

$$B = B^{\mathscr{C}}(T) \equiv -\frac{1}{m_B^{\mathscr{C}}}(T - T_E) + B_E, \tag{2.5}$$

$$C = C^{\mathscr{C}}(T) \equiv -\frac{1}{m_C^{\mathscr{C}}}\left(T - T_E^{AB}\right). \tag{2.6}$$

3. Ternary alloy solidification: mushy layer model

Here we formulate a model for the solidification of a ternary alloy that addresses diffusive transport of heat and solute during solidification in the absence of convection. The basic geometry of this system is set by considering the planar solidification of

a ternary alloy from a cooled boundary at $z = 0$ with temperature T_0 less than the ternary eutectic temperature T_E. As noted above, this leads to the formation of four distinct layers within the system: the liquid layer, the primary mushy layer, the secondary mushy layer and the eutectic solid layer. These four layers are separated by three planar interfaces. We denote the interface between the liquid and the primary mushy layer by $z = h_P(t)$, the interface between the primary mushy layer and the secondary (cotectic) mushy layer by $z = h_S(t)$ and the interface between the secondary mushy layer and the eutectic solid layer by $z = h_E(t)$.

The model that follows is an extension of the binary alloy model presented in Worster (1986). The notation is changed to accommodate the ternary alloy system but the spirit of the analysis is the same. Field equations and boundary conditions for this system can be derived in a manner similar to those for binary alloy solidification in mushy layers (Worster 1986, 1992). For example, solute balances and corresponding solute flux boundary conditions in the ternary mushy layer system can be derived by applying the description in Worster (1992) to the bulk compositions $\bar{B} = \chi B + \phi_B$ and $\bar{C} = \chi C + \phi_C$ where χ is the liquid volume fraction. The dependent variables in our model are the temperature T, the liquid compositions A, B and C, the solid fractions ϕ_A, ϕ_B, ϕ_C, the liquid fraction χ and the interface positions h_P, h_S and h_E.

The conservation equations we present here are the same as those in Krane *et al.* (1997) if in that paper fluid flow is neglected and the segregation (or partition) coefficients are chosen to correspond to solidification of pure phases. The difference between the present model and that of Krane *et al.* is that here we employ an explicit treatment of the three interfaces. In Krane *et al.* boundaries between the different layers are handled implicitly by requiring the differentiability of the liquid fraction throughout a single computational domain that includes liquid and solid regions as well as the mushy regions of primary and secondary solidification. We discuss below how their formulation relates to the present interfacial conditions.

The far-field boundary conditions ($z \to \infty$) in the liquid phase are

$$B = B_\infty, \quad C = C_\infty, \tag{3.1a}$$

$$T = T_\infty. \tag{3.1b}$$

In the liquid where $z > h_P(t)$ the governing equations are

$$\frac{\partial B}{\partial t} = D_B \frac{\partial^2 B}{\partial z^2}, \quad \frac{\partial C}{\partial t} = D_C \frac{\partial^2 C}{\partial z^2}, \tag{3.2a}$$

$$\frac{\partial T}{\partial t} = \kappa \frac{\partial^2 T}{\partial z^2}, \tag{3.2b}$$

$$\chi = 1 \quad (\phi_A = \phi_B = \phi_C = 0), \tag{3.2c}$$

where D_i is the solute diffusivity of species i and κ is the thermal diffusivity in the liquid. We assume that there is negligible cross-coupling between diffusion of heat and species.

The boundary conditions on the liquid–primary mush interface $z = h_P(t)$ are given by

$$L_v \frac{\mathrm{d}h_P}{\mathrm{d}t} [\phi_A]_-^+ = \left[\bar{k} \frac{\partial T}{\partial z} \right]_-^+, \tag{3.3a}$$

$$\frac{\mathrm{d}h_P}{\mathrm{d}t} B [\phi_A]_-^+ = D_B \left[\chi \frac{\partial B}{\partial z} \right]_-^+, \quad \frac{\mathrm{d}h_P}{\mathrm{d}t} C [\phi_A]_-^+ = D_C \left[\chi \frac{\partial C}{\partial z} \right]_-^+, \tag{3.3b}$$

$$[T]^+_- = 0, \tag{3.3c}$$

$$[B]^+_- = [C]^+_- = 0, \tag{3.3d}$$

$$T(h_P, t) = T^{\mathscr{L}}[B(h_P, t), C(h_P, t)], \tag{3.3e}$$

$$\left.\frac{\partial T}{\partial z}\right|^+ = m_B \left.\frac{\partial B}{\partial z}\right|^+ + m_C \left.\frac{\partial C}{\partial z}\right|^+. \tag{3.3f}$$

Here $[\,]^+_-$ indicates the jump in value across the interface and $|^+$ indicates evaluation of the variables in the layer above the interface. We assume that the thermal properties of the different solid phases are the same but that they may differ from those of the liquid phase. In the mushy layers, then, we have a liquid-fraction-weighted thermal conductivity $\bar{k} = \chi k_l + \phi_A k_A + \phi_B k_B + \phi_C k_C = \chi k_l + (1-\chi)k_s$ and a specific heat capacity per unit volume given by $\bar{c} = \chi c_l + (1-\chi)c_s$, where subscript l indicates liquid and subscript s indicates solid. Similarly, we use a single value for the latent heat per unit volume (i.e. $L_v^A = L_v^B = L_v^C \equiv L_v$). The first four conditions (3.3*a–d*) represent conservation and continuity of temperature and solute. Equation (3.3*e*) represents the condition of local thermodynamic equilibrium at the interface and equation (3.3*f*) represents the marginal equilibrium condition. The latter two boundary conditions are straightforward extensions of their binary alloy counterparts (Worster 1986, 1992).

In the primary mushy layer $h_S(t) < z < h_P(t)$ the governing equations are

$$\bar{c}\frac{\partial T}{\partial t} = \frac{\partial}{\partial z}\left[\bar{k}\frac{\partial T}{\partial z}\right] + L_v\frac{\partial \phi_A}{\partial t}, \tag{3.4a}$$

$$\left.\begin{aligned} \chi\frac{\partial B}{\partial t} &= D_B\frac{\partial}{\partial z}\left[\chi\frac{\partial B}{\partial z}\right] + B\frac{\partial \phi_A}{\partial t}, \\ \chi\frac{\partial C}{\partial t} &= D_C\frac{\partial}{\partial z}\left[\chi\frac{\partial C}{\partial z}\right] + C\frac{\partial \phi_A}{\partial t}, \end{aligned}\right\} \tag{3.4b}$$

$$T = T^{\mathscr{L}}(B, C), \tag{3.4c}$$

$$\chi + \phi_A = 1 \quad (\phi_B = \phi_C = 0). \tag{3.4d}$$

The equations in the primary mushy layer are the same as those for the binary alloy case (Worster 1986, 1992) with the exceptions that there are two solute balances rather than one and that the condition of thermodynamic equilibrium in the primary mushy layer (3.4*c*) states that the temperature and liquid compositions lie on the liquidus surface rather than on a liquidus line in the binary case.

The boundary conditions on the mush–mush interface $z = h_S(t)$ are

$$L_v\frac{\mathrm{d}h_S}{\mathrm{d}t}[\phi_A + \phi_B]^+_- = \left[\bar{k}\frac{\partial T}{\partial z}\right]^+_-, \tag{3.5a}$$

$$\left.\begin{aligned} \frac{\mathrm{d}h_S}{\mathrm{d}t}\{B[\phi_A]^+_- + (B-1)[\phi_B]^+_-\} &= D_B\left[\chi\frac{\partial B}{\partial z}\right]^+_-, \\ \frac{\mathrm{d}h_S}{\mathrm{d}t}C\,[\phi_A + \phi_B]^+_- &= D_C\left[\chi\frac{\partial C}{\partial z}\right]^+_-, \end{aligned}\right\} \tag{3.5b}$$

$$[T]^+_- = 0, \tag{3.5c}$$

$$[B]^+_- = [C]^+_- = 0, \tag{3.5d}$$

$$B = B^{\mathscr{C}}(T), \quad C = C^{\mathscr{C}}(T), \tag{3.5e}$$

$$m_B^{\mathscr{C}} \frac{\partial B}{\partial z}\bigg|^{+} = m_C^{\mathscr{C}} \frac{\partial C}{\partial z}\bigg|^{+}. \tag{3.5f}$$

Condition (3.5*e*) indicates that the temperature and compositions on this boundary coincide with the cotectic boundary of the phase diagram. Condition (3.5*f*) represents a condition of marginal equilibrium modified appropriately to apply at the mush–mush interface. Mathematically, this condition states that the solidification path along the liquidus surface joins the cotectic boundary in such a way as to be tangent to that boundary (see solidification paths in figure 4). Physically, this condition ensures that no supersaturation with respect to the second solidifying component (component B) occurs in front of the mush–mush interface. This induces a compositional (diffusive) boundary layer over which the necessary adjustments takes place. We note here that if the solid fractions are continuous across the mush–mush interface then equations (3.5*b*) imply continuous solute gradients across this boundary. Continuity of the solute gradients across the mush–mush interface then directly leads to the condition (3.5*f*) through equation (3.6*c*) below. That is to say, the condition of marginal equilibrium applied to the mush–mush boundary is consistent with the assumption of continuous solid fractions. The model by Krane *et al.* (1997) implicitly applies this marginal equilibrium condition as a consequence of the continuity of the liquid fraction, which was required for the computation of different field equations over a single computational domain. Worster (1986, 2000) argued in favour of the marginal equilibrium condition over the *a priori* assumption of continuous solid fraction in the binary alloy case, noting that (i) a jump in solid fraction (of unity) does occur across a solid–liquid interface and (ii) the interfacial balance conditions for heat and solute incorporate very naturally a jump in solid fraction. The rationale behind the use of the marginal equilibrium conditions is the same for binary and ternary alloys. In the next section we document how the marginal equilibrium condition relates to the jump, or lack thereof, in solid fraction across domain boundaries.

In the secondary mushy layer $h_E(t) < z < h_S(t)$ the governing equations are

$$\bar{c}\frac{\partial T}{\partial t} = \frac{\partial}{\partial z}\left[\bar{k}\frac{\partial T}{\partial z}\right] + L_v \frac{\partial(\phi_A + \phi_B)}{\partial t}, \tag{3.6a}$$

$$\left.\begin{aligned} \chi\frac{\partial B}{\partial t} &= D_B \frac{\partial}{\partial z}\left[\chi\frac{\partial B}{\partial z}\right] + B\frac{\partial \phi_A}{\partial t} + (B-1)\frac{\partial \phi_B}{\partial t}, \\ \chi\frac{\partial C}{\partial t} &= D_C \frac{\partial}{\partial z}\left[\chi\frac{\partial C}{\partial z}\right] + C\frac{\partial(\phi_A + \phi_B)}{\partial t}, \end{aligned}\right\} \tag{3.6b}$$

$$B = B^{\mathscr{C}}(T), \quad C = C^{\mathscr{C}}(T), \tag{3.6c}$$

$$\chi + \phi_A + \phi_B = 1 \quad (\phi_C = 0). \tag{3.6d}$$

Note that in equation (3.6*a*) and also (3.5*a*) it is the rate of change of total solid fraction $\phi_A + \phi_B$ that enters the latent heat term. Also note that the formation of ϕ_B removes an amount of component B from the liquid ($B - 1 < 0$). Equation (3.6*c*) implies that the solidification path follows the cotectic line.

The boundary conditions at the eutectic interface $z = h_E(t)$ are

$$L_v \frac{\mathrm{d}h_E}{\mathrm{d}t}\,[\phi_A + \phi_B + \phi_C]_{-}^{+} = \left[\bar{k}\frac{\partial T}{\partial z}\right]_{-}^{+}, \tag{3.7a}$$

$$\left.\begin{aligned}\frac{\mathrm{d}h_E}{\mathrm{d}t}\left\{B\,[\phi_A]_-^+ + (B-1)\,[\phi_B]_-^+ + B\,[\phi_C]_-^+\right\} &= D_B\left[\chi\frac{\partial B}{\partial z}\right]_-^+,\\ \frac{\mathrm{d}h_E}{\mathrm{d}t}\left\{C\,[\phi_A]_-^+ + C\,[\phi_B]_-^+ + (C-1)\,[\phi_C]_-^+\right\} &= D_C\left[\chi\frac{\partial C}{\partial z}\right]_-^+,\end{aligned}\right\} \tag{3.7b}$$

$$[T]_-^+ = 0, \tag{3.7c}$$

$$T = T_E, \tag{3.7d}$$

$$B = B_E, \quad C = C_E. \tag{3.7e}$$

In the solid phase $0 < z < h_E(t)$ there is thermal diffusion

$$\frac{\partial T}{\partial t} = \kappa_s\frac{\partial^2 T}{\partial z^2}, \tag{3.8a}$$

$$\phi_A + \phi_B + \phi_C = 1 \quad (\chi = 0). \tag{3.8b}$$

Note that with the assumption of no solid solutions, $\bar{A} = \chi A + \phi_A$, $\bar{B} = \chi B + \phi_B$ and $\bar{C} = \chi C + \phi_C$, so that in the eutectic solid where $\chi = 0$ we have $\bar{A} = \phi_A$, $\bar{B} = \phi_B$ and $\bar{C} = \phi_C$.

On $z = 0$

$$T = T_0, \tag{3.9}$$

where $T_0 < T_E$.

4. Mushy layer model reduction

In this section we first reformulate the above problem in terms of a similarity variable and then outline the solution method used to solve the resulting system numerically.

4.1. *Similarity formulation*

We seek a similarity solution to the ternary mushy layer model by introducing the variable

$$\eta = \frac{z}{2\sqrt{\kappa t}}, \tag{4.1}$$

where we also seek interface positions of the form

$$h_P(t) = 2\lambda_P\sqrt{\kappa t}, \quad h_S(t) = 2\lambda_S\sqrt{\kappa t}, \quad h_E(t) = 2\lambda_E\sqrt{\kappa t}. \tag{4.2}$$

Here λ_P, λ_S and λ_E are dimensionless constants to be determined. They represent the interface positions with respect to the similarity variable η.

In the liquid layer ($\eta > \lambda_P$) the temperature and compositions can be expressed in terms of complementary error functions

$$T = T_\infty + \frac{(T_P - T_\infty)\,\mathrm{erfc}(\eta)}{\mathrm{erfc}(\lambda_P)}, \tag{4.3a}$$

$$B = B_\infty + \frac{(B_P - B_\infty)\,\mathrm{erfc}(\delta_B\eta)}{\mathrm{erfc}(\delta_B\lambda_P)}, \tag{4.3b}$$

$$C = C_\infty + \frac{(C_P - C_\infty)\,\mathrm{erfc}(\delta_C\eta)}{\mathrm{erfc}(\delta_C\lambda_P)}, \tag{4.3c}$$

where T_P, B_P and C_P are the interface temperature and compositions to be determined. Here $\delta_i^2 = \kappa/D_i$ is a thermal to solute diffusivity ratio ($i = B, C$), which is typically large.

Similarly, in the solid layer ($0 \leqslant \eta < \lambda_E$) the temperature field is given by

$$T = T_0 + (T_E - T_0)\frac{\operatorname{erf}(\delta_s \eta)}{\operatorname{erf}(\delta_s \lambda_E)}, \tag{4.4}$$

where $\delta_s^2 = \kappa/\kappa_s$ is the ratio of thermal diffusivities in the liquid and solid. The corresponding temperature gradient in the solid at the eutectic front is

$$\left.\frac{\mathrm{d}T}{d\eta}\right|^{E^-} = \frac{2\delta_s^2 \lambda_E (T_E - T_0)}{G(\delta_s \lambda_E)}, \tag{4.5}$$

where

$$G(x) \equiv \pi^{1/2} x \exp(x^2) \operatorname{erf}(x). \tag{4.6}$$

We now focus on the remaining equations and boundary conditions associated with the two mushy layers. Using equations (4.3) and boundary conditions (3.3*e*, *f*) we find that B_P and C_P are related by

$$1 = \frac{B_P - B_\infty}{W_B(\lambda_P)} + \frac{C_P - C_\infty}{W_C(\lambda_P)}, \tag{4.7}$$

where

$$W_i(\lambda) \equiv \frac{(-\Delta T_\infty/m_i) F(\delta_i \lambda)}{\delta_i^2 F(\lambda) - F(\delta_i \lambda)} \qquad (i = B, C), \tag{4.8}$$

and

$$\Delta T_\infty \equiv T_\infty - T^{\mathscr{L}}(B_\infty, C_\infty), \tag{4.9a}$$

$$F(x) \equiv \pi^{1/2} x \exp(x^2) \operatorname{erfc}(x). \tag{4.9b}$$

It is also possible to combine the three flux boundary conditions (3.3*a*,*b*) using equations (3.3*f*) and (3.4*c*) to show that the value of the liquid fraction $\chi = \chi^{P^-}$ on $\eta = \lambda_P$ in the primary mushy layer satisfies $(1 - \chi^{P^-})(\chi^{P^-} - \chi^{P^\star}) = 0$ where

$$\chi^{P^\star} = \frac{\bar{m}_B \delta_B^2 B_\infty \left[1 - \dfrac{B_P - B_\infty}{J_B(\lambda_P)}\right] + \bar{m}_C \delta_C^2 C_\infty \left[1 - \dfrac{C_P - C_\infty}{J_C(\lambda_P)}\right]}{\gamma \delta_s^2 + (1 - k_l/k_s)\left(\bar{m}_B \delta_B^2 B_P + \bar{m}_C \delta_C^2 C_P\right)}. \tag{4.10}$$

Here we have defined

$$J_B(\lambda) = \frac{B_\infty F(\delta_B \lambda)}{1 - F(\delta_B \lambda)}, \quad J_C(\lambda) = \frac{C_\infty F(\delta_C \lambda)}{1 - F(\delta_C \lambda)}, \tag{4.11}$$

and

$$\bar{m}_i = \frac{m_i}{m_B + m_C} \quad (i = B, C), \tag{4.12a}$$

$$\gamma = \frac{L_v}{c_s(m_B + m_C)}. \tag{4.12b}$$

When $0 \leqslant \chi^{P^\star} < 1$ only the choice $\chi^{P^-} = \chi^{P^\star}$ leads to a physically valid solution. When $\chi^{P^\star}$ is not in this interval $\chi^{P^-} = 1$ applies. This follows, in a similar manner to that in Worster (1986) for a binary alloy, by requiring $\mathrm{d}\chi/\mathrm{d}\eta > 0$ at P^-($\mathrm{d}\chi/\mathrm{d}\eta$ derived from equations (4.15)). Therefore, we interpret the condition on the liquid fraction as

$$\chi^{P^-} = \begin{cases} \chi^{P^\star} & \text{if } 0 \leqslant \chi^{P^\star} < 1 \\ 1 & \text{otherwise.} \end{cases} \tag{4.13}$$

This result indicates the possibility of a jump in the liquid fraction at the liquid–mush interface. The two flux conditions on $\eta = \lambda_P$ that remain are expressed as

$$\left.\begin{aligned} \chi^{P^-}\left.\frac{\mathrm{d}B}{\mathrm{d}\eta}\right|^{P^-} &= 2\delta_B^2\lambda_P\left[B_P(1-\chi^{P^-}) - \frac{(B_P - B_\infty)}{F(\delta_B\lambda_P)}\right], \\ \chi^{P^-}\left.\frac{\mathrm{d}C}{\mathrm{d}\eta}\right|^{P^-} &= 2\delta_C^2\lambda_P\left[C_P(1-\chi^{P^-}) - \frac{(C_P - C_\infty)}{F(\delta_C\lambda_P)}\right]. \end{aligned}\right\} \tag{4.14}$$

The governing equations in the primary mushy layer can be reduced to

$$-\bar{c}\eta\left(m_B\frac{\mathrm{d}B}{\mathrm{d}\eta} + m_C\frac{\mathrm{d}C}{\mathrm{d}\eta}\right) = \frac{1}{2\kappa}\frac{\mathrm{d}}{\mathrm{d}\eta}\left[\bar{k}\left(m_B\frac{\mathrm{d}B}{\mathrm{d}\eta} + m_C\frac{\mathrm{d}C}{\mathrm{d}\eta}\right)\right] + L_v\eta\frac{\mathrm{d}\chi}{\mathrm{d}\eta}, \tag{4.15a}$$

$$-2\delta_B^2\eta\frac{\mathrm{d}(\chi B)}{\mathrm{d}\eta} = \frac{\mathrm{d}}{\mathrm{d}\eta}\left[\chi\frac{\mathrm{d}B}{\mathrm{d}\eta}\right], \quad -2\delta_C^2\eta\frac{\mathrm{d}(\chi C)}{\mathrm{d}\eta} = \frac{\mathrm{d}}{\mathrm{d}\eta}\left[\chi\frac{\mathrm{d}C}{\mathrm{d}\eta}\right], \tag{4.15b}$$

for the dependent variables B, C and χ. The remaining dependent variables can be obtained explicitly using

$$T = T^{\mathscr{L}}(B, C), \tag{4.16a}$$

$$\phi_A = 1 - \chi. \tag{4.16b}$$

We next examine the boundary conditions at the mush–mush interface. The heat flux balance condition (3.5a) and the two solute flux balance conditions (3.5b) can be manipulated using the cotectic condition (3.6c) and the marginal equilibrium condition (3.5f) to obtain three equivalent relations. The first two of these give conditions on the values of χ and ϕ_B in the secondary mushy layer at this boundary:

$$\chi^{S^-} = \begin{cases} \chi^{S^\star} & \text{if } 0 \leqslant \chi^{S^\star} < \chi^{S^+} \\ \chi^{S^+} & \text{otherwise,} \end{cases} \tag{4.17a}$$

$$\phi_B^{S^-} = (\chi^{S^+} - \chi^{S^-})\left[B_S - \frac{\delta_C^2 m_C^{\mathscr{C}}}{\delta_B^2 m_B^{\mathscr{C}}}C_S\right], \tag{4.17b}$$

where

$$\chi^{S^\star} = \frac{-\delta_C^2\dfrac{m_C^{\mathscr{C}}}{m_B^{\mathscr{C}}}C_S - \dfrac{1}{2\lambda_S}\left.\dfrac{dB}{d\eta}\right|^{S^+}}{\gamma_B\delta_s^2 - \delta_C^2\dfrac{m_C^{\mathscr{C}}}{m_B^{\mathscr{C}}}\left(1 - \dfrac{k_l}{k_s}\right)C_S}, \tag{4.18}$$

and

$$\gamma_B \equiv \frac{L_v}{m_B^{\mathscr{C}}c_s} = \frac{m_B + m_C}{m_B^{\mathscr{C}}}\gamma. \tag{4.19}$$

The choices represented in equation (4.17a) follow by requiring $\mathrm{d}\chi/\mathrm{d}\eta > 0$ at S^- ($\mathrm{d}\chi/\mathrm{d}\eta$ calculated using equations (4.23)). In particular, we note that when $0 \leqslant \chi^{S^\star} < \chi^{S^+}$ the choice $\chi^{S^-} = \chi^{S^+}$ leads to a non-physical solution. The remaining condition may be expressed as

$$\chi^{S^-}\left.\frac{\mathrm{d}B}{\mathrm{d}\eta}\right|^{S^-} = \chi^{S^+}\left.\frac{\mathrm{d}B}{\mathrm{d}\eta}\right|^{S^+} + 2\delta_C^2\lambda_S\frac{m_C^{\mathscr{C}}}{m_B^{\mathscr{C}}}C_S(\chi^{S^+} - \chi^{S^-}). \tag{4.20}$$

The two cotectic conditions (3.5*e*) give the interface temperature and a relation between the compositions B_S and C_S given by

$$C_S - \frac{m_B^{\mathscr{C}}}{m_C^{\mathscr{C}}}(B_S - B_E) - C_E = 0. \tag{4.21}$$

The marginal equilibrium condition (3.5*f*) is expressed as

$$m_B^{\mathscr{C}} \left.\frac{\mathrm{d}B}{\mathrm{d}\eta}\right|^{S^+} - m_C^{\mathscr{C}} \left.\frac{\mathrm{d}C}{\mathrm{d}\eta}\right|^{S^+} = 0. \tag{4.22}$$

A reduced set of governing equations in the secondary mushy layer for the variables B and χ can be derived. The two solute fields B and C and the temperature are directly related by the cotectic relation (3.6*c*). This allows us to combine the two solute balance equations (3.6*b*) into one that is integrable. This gives an explicit solution for ϕ_B in terms of χ and B (see equation (4.24*b*)). The equations in the secondary mushy layer are then

$$\frac{\mathrm{d}}{\mathrm{d}\eta}\left[\bar{k}\frac{\mathrm{d}B}{\mathrm{d}\eta}\right] = -2\kappa\bar{c}\eta\frac{\mathrm{d}B}{\mathrm{d}\eta} + \frac{2\kappa L_v}{m_B^{\mathscr{C}}}\eta\frac{\mathrm{d}\chi}{\mathrm{d}\eta}, \tag{4.23a}$$

$$\frac{\mathrm{d}}{\mathrm{d}\eta}\left[\chi\frac{\mathrm{d}B}{\mathrm{d}\eta}\right] = -2\delta_C^2\eta\frac{\mathrm{d}}{\mathrm{d}\eta}\left[\chi\left(B - B_E^{AB}\right)\right], \tag{4.23b}$$

where the remaining dependent variables are given explicitly by

$$C = \frac{m_B^{\mathscr{C}}}{m_C^{\mathscr{C}}}(B - B_E) + C_E = \frac{m_B^{\mathscr{C}}}{m_C^{\mathscr{C}}}\left(B - B_E^{AB}\right), \tag{4.24a}$$

$$\phi_B = \phi_B^{S^-} + (\chi B - \chi^{S^-} B_S)\left(\frac{\delta_C^2}{\delta_B^2} - 1\right) - \frac{\delta_C^2}{\delta_B^2}(\chi - \chi^{S^-})B_E^{AB}, \tag{4.24b}$$

$$T = -m_B^{\mathscr{C}}(B - B_E) + T_E, \tag{4.24c}$$

$$\phi_A = 1 - \chi - \phi_B. \tag{4.24d}$$

We next examine the conditions at the eutectic boundary $\eta = \lambda_E$. The three flux conditions (3.7*a*,*b*) can be simplified using equations (3.6*c*), (4.4) and (4.5) to obtain the three conditions

$$2L_v\kappa\lambda_E\chi^{E^+} = \frac{2k_s\delta_s^2\lambda_E(T_E - T_0)}{G(\delta_s\lambda_E)} - \bar{k}^{E^+}\left.\frac{\mathrm{d}T}{\mathrm{d}\eta}\right|^{E^+}, \tag{4.25a}$$

$$-2\delta_B^2\lambda_E\left(B_E\chi^{E^+} + \phi_B^{E^+} - \phi_B^{E^-}\right) = \chi^{E^+}\left.\frac{\mathrm{d}B}{\mathrm{d}\eta}\right|^{E^+}, \tag{4.25b}$$

$$-2\delta_C^2\lambda_E\left(C_E\chi^{E^+} - \phi_C^{E^-}\right) = \chi^{E^+}\left.\frac{\mathrm{d}C}{\mathrm{d}\eta}\right|^{E^+}, \tag{4.25c}$$

where we note that $\phi_C^{E^+} = 0$. Equations (4.25*b*,*c*) determine the quantities $\phi_B^{E^-}$ and $\phi_C^{E^-}$, that is the solid fractions in the eutectic solid. Solving gives

$$\phi_B^{E^-} = \phi_B^{E^+} + \chi^{E^+}\left(B_E + \frac{1}{2\delta_B^2\lambda_E}\left.\frac{\mathrm{d}B}{\mathrm{d}\eta}\right|^{E^+}\right), \tag{4.26a}$$

$$\phi_C^{E^-} = \chi^{E^+}\left(C_E + \frac{1}{2\delta_C^2\lambda_E}\left.\frac{\mathrm{d}C}{\mathrm{d}\eta}\right|^{E^+}\right), \tag{4.26b}$$

and $\phi_A^{E^-} = 1 - \phi_B^{E^-} - \phi_C^{E^-}$. Equations (4.26) reduce to the expected results in the absence of solute diffusion or when the compositions are uniform. In that case we know from the ternary phase diagram that the remaining liquid at the eutectic point solidifies into solids with proportions $A_E : B_E : C_E$. These proportions add to the solid fractions already present (namely $\phi_A^{E^+}$ and $\phi_B^{E^+}$) at the eutectic point. The inclusion of solute diffusion accounts for the possibility that there is either an enhancement or a reduction of solute available to be incorporated into the eutectic solid due to diffusion of solute towards or away from the eutectic boundary in the remaining liquid. The third flux balance (4.25*a*) can be expressed, using equation (4.24*c*), as

$$\left.\frac{\mathrm{d}B}{\mathrm{d}\eta}\right|^{E^+} = \frac{2\lambda_E \gamma_B \delta_s^2}{1 + (k_s/k_l - 1)\,\chi^{E^+}} \left(\chi^{E^+} - \frac{S_0}{G(\delta_s \lambda_E)} \right), \tag{4.27}$$

where

$$S_0 = \frac{c_s(T_E - T_0)}{L_v} = \frac{T_E - T_0}{\gamma(m_B + m_C)}. \tag{4.28}$$

Finally, at the eutectic boundary we require that $B = B_E$ so that $T = T_E$ and $C = C_E$ on $\eta = \lambda_E$ as required by equations (4.24*a*,*c*).

4.2. *Solution method for the diffusion case*

Our solution method for this coupled differential free-boundary problem is similar to the approach for the binary alloy model of Worster (1986). Integration of the governing equations is performed for initially guessed interface positions and interface quantities. After integration, residual boundary conditions are evaluated and the guesses are updated in an iterative procedure to ultimately converge to a solution satisfying the governing equations and all boundary conditions.

In particular, we begin by guessing values for the six quantities λ_P, λ_S, λ_E, B_P, B_S and χ^{E^+}. The governing equations in the primary mushy layer (4.15) and secondary mushy layer (4.23) are then solved subject to the boundary conditions $B = B_P$, $C = C_P$ and $\chi = \chi^{P^-}$ at $\eta = \lambda_P$, $B = B_S$ and $C = C_S$ at $\eta = \lambda_S$ and $B = B_E$ and $\chi = \chi^{E^+}$ at $\eta = \lambda_E$, where the quantities C_P, χ^{P^-} and C_S are obtained from equations (4.7), (4.13) and (4.21). We then iterate on the six guessed quantities in order to satisfy residual boundary conditions. These six residuals are given by the two solute flux conditions at λ_P (equations (4.14)), the value of χ in the secondary mushy layer at the cotectic boundary (equation (4.17*a*)), the solute flux condition for B at the cotectic boundary (equation (4.20)), the modified marginal equilibrium condition (equation (4.22)), and the flux balance at $\eta = \lambda_E$ (equation (4.27)).

We have implemented a numerical procedure to carry out the above computations. The nonlinear solve component for the six-dimensional parameter space uses the code hybrd.f, which is based on a modification of the Powell hybrid method, and is available in the MINPACK package at NETLIB. Inside each of the iterative steps in this nonlinear solve the two systems of differential equations given in equations (4.15) and (4.23) are solved using a simple Jacobi iteration for the composition equations and quadrature (trapezoid rule) for the liquid fraction equations. Second-order-accurate uniform spatial discretization has been used and our computed solutions have been checked to satisfy the differential equations and residual boundary conditions to within an error of order 10^{-7}. The majority of the calculations have used 200 uniformly spaced grid points in each mushy layer, although we have checked convergence using 400 and 800 points. We note that a typical calculation with 200 grid points

has approximately 20 points in the solutal boundary layer above the mush–mush interface.

5. Solution with zero solute diffusion and zero latent heat

Before presenting the results of the above computations for the full model, we address a simplified case in which an analytical solution is possible. In particular, we consider the case where solute diffusion is zero ($\delta_i \to \infty$ for $i = B, C$), latent heat is zero ($\gamma \to 0$ and $S_0 \to \infty$ with γS_0 fixed), and the thermal properties in the solid and liquid phases are equal. While these assumptions may not be realistic for many physical systems, we present this analytical solution as a valuable tool for use in finding and verifying other more complicated solutions.

In the limit of zero solute diffusion, compositional boundary layers are unresolved. In addition to the absence of solute diffusion terms ($D_i = 0$) in the field equations and interfacial conditions, there is an effective reinterpretation of the marginal equilibrium conditions, as described in Worster (2002). At the liquid–mush interface the marginal equilibrium condition (3.3*f*) reduces to $T = T^{\mathscr{L}}(B, C)$ on the liquid side of the interface; this leads to continuous solute fields across the now unresolved compositional boundary layer. Similarly, the boundary layer in the primary mush at the mush–mush interface over which the solute field adjusts to avoid supersaturation (represented by the condition (3.5*f*)) is unresolved in the limit of zero solute diffusion and marginal equilibrium in this context then requires that the temperature in the primary mushy layer at the mush–mush interface corresponds to the cotectic temperature in equation (3.5*e*). The compositional fields in the primary mushy layer follow a tie-line all the way to the cotectic boundary.

With these ideas in mind we proceed to solve the equations in this limit. In the absence of solute diffusion, the bulk compositions in each layer are constant. Further, the solute flux interface conditions (3.3*b*), (3.5*b*) and (3.7*b*) imply that there is no jump in the bulk composition at a moving interface. This implies that $\bar{B} = B_\infty$ and $\bar{C} = C_\infty$ in each of the layers. We can use this to obtain expressions for the liquid composition throughout the system as well as the solid fractions in the solid layer. In the liquid layer

$$B = B_\infty, \quad C = C_\infty. \tag{5.1}$$

In the primary mushy layer

$$B = \frac{B_\infty}{\chi}, \quad C = \frac{C_\infty}{\chi}. \tag{5.2}$$

In the secondary mushy layer

$$B = \frac{B_\infty - \phi_B}{\chi}, \quad C = \frac{C_\infty}{\chi}. \tag{5.3}$$

In the eutectic solid layer

$$\phi_B = B_\infty, \quad \phi_C = C_\infty, \quad \phi_A = 1 - \phi_B - \phi_C. \tag{5.4}$$

Owing to the continuity of temperature at the interfaces and the coupling of temperature and solute in the mushy layers through the liquidus and cotectic relations, the liquid compositions and the solid fractions are continuous across the interfaces. In particular, at the primary mush–liquid interface the condition of continuous temperature (3.3*c*), the two equilibrium conditions (3.3*e*) and (3.4*c*)

along with equations (5.1) and (5.2) require that $\phi_A^{P^-} = 0$ so that there is no jump in the solid fraction at the liquid–mush interface. It then follows from equations (5.1) and (5.2) that the liquid compositions are continuous across the liquid–mush interface. Similarly, it follows from conditions (3.5*c*), (3.5*e*) and (3.6*c*) along with equations (5.2) and (5.3) that $\chi^{S^-} = \chi^{S^+}$ (see equation (5.8)), $\phi_B^{S^-} = 0$ and that the liquid compositions are continuous across the mush–mush interface. There is a jump in liquid fraction across the eutectic boundary and one can show using equations (5.3) and (3.7*e*) that $\chi^{E^+} = C_\infty / C_E$.

The thermal field, which also decouples, can be written down explicitly. In particular, owing to the assumption of equal thermal properties in each phase and the assumption of zero latent heat, the thermal field satisfies the same heat equation in each layer and is subject to continuity of temperature and heat flux at the layer boundaries. Consequently, the thermal field throughout the system ($0 < \eta < \infty$) can be expressed as

$$T = T_0 + (T_\infty - T_0)\,\mathrm{erf}(\eta). \tag{5.5}$$

The resulting interface positions λ_P, λ_S and λ_E can be determined from equation (5.5) in terms of the corresponding interface temperatures T_P, T_S and T_E:

$$\mathrm{erf}(\lambda_P) = \frac{T_P - T_0}{T_\infty - T_0}, \quad \mathrm{erf}(\lambda_S) = \frac{T_S - T_0}{T_\infty - T_0}, \quad \mathrm{erf}(\lambda_E) = \frac{T_E - T_0}{T_\infty - T_0}. \tag{5.6}$$

Equation (3.3*e*) determines the value of T_P while the two cotectic conditions (3.5*e*) determine T_S and χ^{S^+}:

$$T_P = T^{\mathscr{L}}(B_\infty, C_\infty), \tag{5.7a}$$

$$T_S = T_E^{AB} - \frac{m_C^{\mathscr{C}} C_\infty}{\chi^{S^+}}, \tag{5.7b}$$

$$\chi^{S^+} = \frac{B_\infty - \left(m_C^{\mathscr{C}}/m_B^{\mathscr{C}}\right) C_\infty}{B_E^{AB}}. \tag{5.8}$$

Finally, we can obtain expressions for the liquid and solid fractions in the two mushy layers through the conditions of thermodynamic equilibrium. In the primary mushy layer we use the expressions for temperature (5.5) and compositions (5.2) in equation (3.4*c*) to obtain

$$\chi = \frac{m_B B_\infty + m_C C_\infty}{T - T_M} = \frac{T^{\mathscr{L}}(B_\infty, C_\infty) - T_M}{T - T_M}, \quad \lambda_S \leqslant \eta \leqslant \lambda_P, \tag{5.9}$$

with $\phi_A = 1 - \chi$, $\phi_B = 0$ and $\phi_C = 0$. In the secondary mushy layer we use the expressions for temperature (5.5) and compositions (5.3) in equations (3.6*c*) to obtain

$$\chi = \frac{m_C^{\mathscr{C}} C_\infty}{T_E^{AB} - T}, \quad \lambda_E \leqslant \eta \leqslant \lambda_S, \tag{5.10a}$$

$$\phi_B = B_\infty - \chi \left(B_E - \frac{T - T_E}{m_B^{\mathscr{C}}} \right), \quad \lambda_E \leqslant \eta \leqslant \lambda_S, \tag{5.10b}$$

with $\phi_A = 1 - \chi - \phi_B$ and $\phi_C = 0$.

6. Results

We now examine the results of the numerical calculations of the full model. For each set of input parameters we find the three interface positions and the

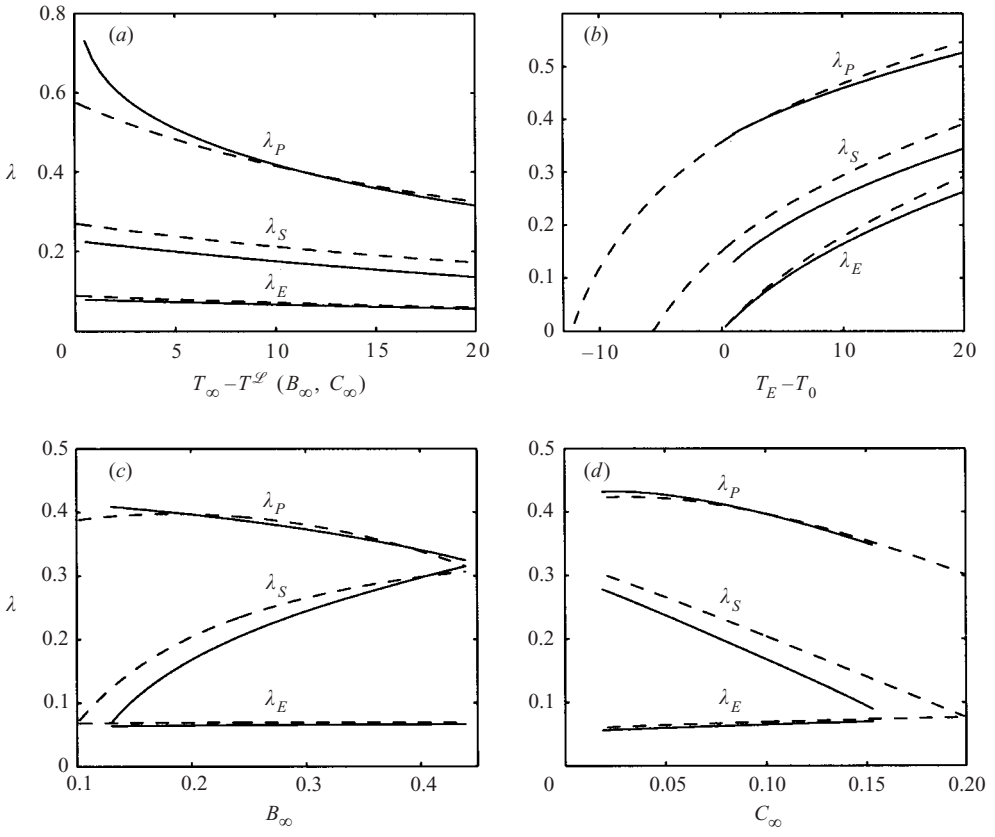

FIGURE 2. The dependence of the interface positions λ_P, λ_S and λ_E on the control parameters T_∞, T_0, B_∞ and C_∞. The solid lines correspond to the numerically calculated values using parameters given in table 1 and the dashed lines correspond to the global model results of Thompson *et al.* described in the Appendix. We note that their model allows predictions above the eutectic temperature and so the $T_E - T_0$ values are extended accordingly.

corresponding temperature, composition and solid fraction profiles through the layers. We compare these solutions with the analytical solution given above, the experimental measurements of Aitta *et al.*, and the global model results of Thompson, Huppert & Worster described in the Appendix.

The interface positions λ_P, λ_S and λ_E (see equations (4.2)) depend in a complicated way on the material and control parameters of the system. In figure 2 the calculated values of λ_P, λ_S and λ_E are shown as the four control parameters T_∞, T_0, B_∞ and C_∞ are individually varied. The solid lines correspond to the calculations based on the full model above while the dashed lines correspond to the results from the global model by Thompson *et al.* described in the Appendix. The parameters not varied in each figure are held fixed at the values listed in case (*a*) of table 1.

Figure 2(*a*) shows the effect of varying T_∞, or the superheat $T_\infty - T^{\mathscr{L}}(B_\infty, C_\infty)$. The superheat most strongly affects the growth of the primary mushy layer interface, λ_P; the cotectic and eutectic interface positions change relatively little. In particular, as the limit of zero superheat is approached heat flux from the liquid is unable to limit growth and a weak logarithmic singularity develops (Worster 1991). This effect is not

	Case (*a*)	Aitta *et al.* exp. 6	Aitta *et al.* exp. 7
B_E	1/3	0.37	0.06
C_E	1/3	0.06	0.37
B_E^{AB}	0.5	0.38	0.10
T_E (°C)	−19	−19	−19
T_E^{AB} (°C)	−5	−16.4	−5
T_M (°C)	0	0	0
δ_B	10	15	15
δ_C	10	15	15
δ_s	1	0.33	0.33
k_l/k_s	1	0.25	0.25
c_l/c_s	1	2.26	2.26
γ	−1	−1.79	−1.79
B_∞	0.2	0.146	0.035
C_∞	0.1	0.012	0.152
T_∞ (°C)	5	20	20
T_0 (°C) [S_0]	−22.078 [0.054]	−27.7 [0.052]	−23.3 [0.026]
λ_P (full model)	0.397	0.581	0.463
λ_S (full model)	0.168	0.313	0.255
λ_E (full model)	0.0648	0.284	0.177
λ_P (analytical)	0.556	0.408	0.317
λ_S (analytical)	0.292	0.187	0.147
λ_E (analytical)	0.101	0.163	0.0882
λ_P (experiment)	–	0.570	0.496
λ_S (experiment)	–	0.211	0.166
λ_E (experiment)	–	0.166	0.0739

TABLE 1. Three sets of material parameters, experimental control parameters, and λ value results (full one-dimensional model, analytical solution and experiments of Aitta *et al.*). The data in the first column corresponds to a symmetric phase diagram. Those in the second column have been chosen based on the phase diagram information and experimental control parameters corresponding to experiment 6 of Aitta *et al.* Here we interpret B as the composition of $NaNO_3$ and C as the composition of KNO_3. The data in the third column has been chosen based on the phase diagram information and experimental control parameters corresponding to experiment 7 of Aitta *et al.* Here B and C are interpreted as the compositions of KNO_3 and $NaN0_3$, respectively. In these last two cases we have approximated the material parameters δ_s, k_l/k_s, c_l/c_s and L_v to be those for water/ice. The value for γ in this case uses $L_v/c_s = 167°C$. The experimental λ values were calculated from the a values in Aitta *et al.* using their quoted value for the thermal diffusivity $\kappa = 1.1 \times 10^{-3}\,\mathrm{cm}^2\,\mathrm{s}^{-1}$.

present in the global model results (dashed curve) since the latent heat in that case is effectively released at the interface (see Appendix).

Reduction of the base temperature T_0, as shown figure 2(b), causes an increase in the three interface positions. In terms of the thickness of each layer, however, the eutectic solid layer is most strongly influenced by the base temperature; growth occurs subject to a balance between latent heat release at the eutectic isotherm and heat conduction through the solid. In contrast, the thicknesses of the secondary mushy layer and the primary mushy layer decrease slightly with decreasing plate temperature. This can be explained by noting that while reduction in the base temperature increases the overall temperature difference across the system, this increased difference (and hence increased layer thickness) is primarily across the eutectic solid; the temperature differences across either mushy layer are compositionally controlled through compositional differences between points P, S and E in the phase diagram (see figure 1). As $T_E - T_0 \to 0$ the growth of eutectic solid correspondingly vanishes while the mushy

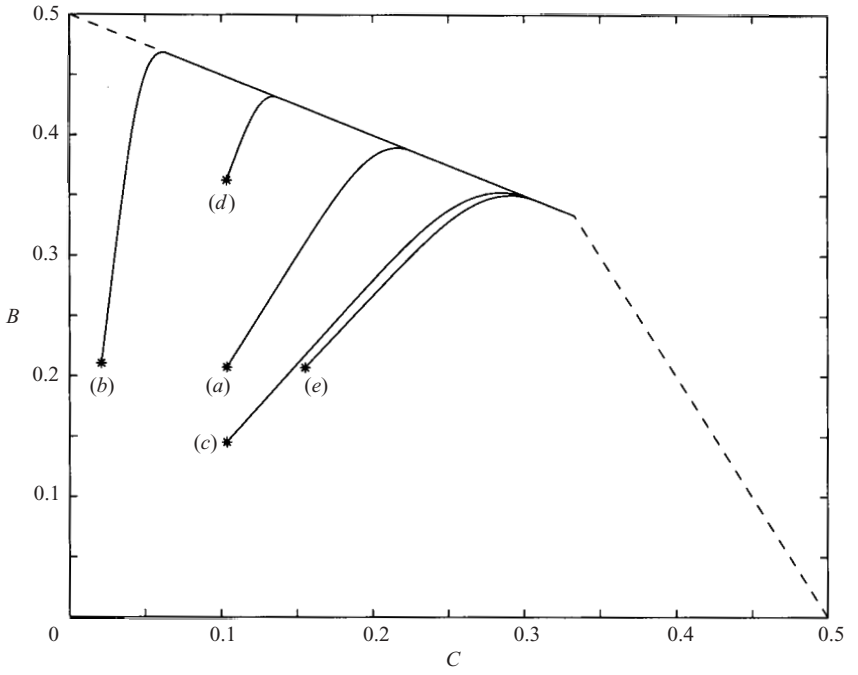

FIGURE 3. Solidification paths in the B–C plane. The parameter values for case (a) are those listed in table 1. The parameter values for cases (b)–(e) are the same as case (a) with the exception that different far-field compositions B_∞ and C_∞ for each path are used. Case (b) has $B_\infty = 0.2$ and $C_\infty = 0.02$, case (c) has $B_\infty = 0.14$ and $C_\infty = 0.1$, case (d) has $B_\infty = 0.35$ and $C_\infty = 0.1$ and case (e) has $B_\infty = 0.2$ and $C_\infty = 0.15$. The temperature, solute and solid fraction profiles for case (a) are shown in figure 5.

layer thicknesses remain relatively unchanged. The global model results of Thompson *et al.* from the Appendix, which are shown by the dashed curves, may be applied for base temperatures above the eutectic temperature so the values of $T_E - T_0$ are extended accordingly.

The two mushy layer thicknesses vary strongly with the far-field compositions B_∞ and C_∞ as shown in figure 2(c,d). Note that we fix T_∞ here so that the superheat $T_\infty - T^{\mathscr{L}}(B_\infty, C_\infty)$ varies through the dependence of the liquidus temperature on the compositions. As B_∞ is decreased λ_S approaches λ_E, indicating the thinning of the secondary mushy layer (see figure 2c). Similarly, as B_∞ is increased the primary mushy layer thins. We can recognize these two limits in corresponding solidification paths in the ternary phase diagram. For example, for case (c) in figure 3 the secondary mushy layer is relatively thin while for case (d) the primary mushy layer is relatively thin. A thin primary mushy layer indicates close proximity of B_∞ and C_∞ to the cotectic line and that relatively little solid ϕ_A needs to be removed before the liquid composition reaches that along the cotectic line. Likewise, a thin secondary mushy layer indicates the close proximity of the far-field compositions to a tie-line connecting the A corner to the eutectic point. In that case, solidification along the liquidus surface (primary mush) proceeds until the compositions reach the cotectic line. Following this, relatively little solidification in the secondary mush (removing solid A and B) is required before the eutectic reaction takes place. Related trends with respect to the far-field composition C_∞ are shown in figure 2(d) and corresponding solidification

paths ranging from case (*b*) to case (*e*) are shown in figure 3. For the reasons described above, we can conclude from figure 2 that the eutectic interface position λ_E is sensitive only to the base temperature while the other interface positions λ_S and λ_P are subject to both thermal and compositional control. The results in figure 2 show that the relative thicknesses of the primary and secondary mushy layers can vary broadly; parameter regimes exist in which the primary mushy layer is very thin compared to the secondary mushy layer and vice versa. These geometrical properties may play important roles in the type of convection that may occur in these layers.

Figure 2 shows good agreement between the present model and the global model of Thompson *et al.* One notable difference between the predictions of the two models occurs at low superheat; a physical interpretation of this is given in the Appendix. Also, the relatively large difference in the predictions of the secondary interface position λ_S can be related to the different values of solute diffusivity used in the two models. The model of Thompson *et al.* has zero solute diffusion while for the calculations with the present model the solutal to thermal diffusivity ratio is 10^{-2}. Of the three interface positions, λ_S varies most strongly with the solute diffusivity and we note that a decrease in the solute diffusivity in the full model closes the gap between the predictions for λ_S. Correspondingly, we note that the value of B_∞ (see figure 2*c*) at which the secondary mushy layer has zero thickness is larger than that predicted by the global model (which is $B_\infty = C_\infty$ for the symmetric case shown). In the full model with solute diffusion this would correspond to a solidification path in figure 3 (starting at a value of B_∞ slightly above the line $B = C$) that reaches the eutectic point without first intersecting the cotectic line. Physically, the mush–mush interface λ_S responds to the rate, determined by the thickness of the solutal boundary layer above the mush–mush interface, at which the departure from the tie-line along the liquidus surface takes place. The sensitivity of the solidification paths to the solute diffusivity is shown in figure 4.

As noted above, some of the character of solidification in the primary and secondary mushy layers is captured in the solidification paths drawn in the B–C plane. Figure 3 shows such solidification paths corresponding to different values of B_∞ and C_∞. Primary solidification occurs at temperatures and compositions on the liquidus surface while secondary solidification occurs at temperatures and compositions on a cotectic line (the dashed lines indicate the positions of two cotectic lines). Note that the starting values along the paths shown are the values of B_P and C_P, which differ slightly from B_∞ and C_∞ owing to a diffusive solutal boundary layer at the liquid–primary mushy layer interface (these differences can be observed in the composition profiles of figure 5). Each solidification path follows predominantly a tie-line as it traverses the liquidus surface, then joins smoothly to the cotectic line and follows the cotectic line until it reaches the eutectic point. In our simplified ternary phase diagram solid phase A (in the experiments of Aitta *et al.* this is the pure ice phase), which solidifies out in the primary mushy layer, incorporates no solute and causes the liquid compositions B and C to increase at constant proportion. This is always true when solute diffusion is absent; in that case the solidification path through the primary mushy layer is the tie-line. When solute diffusion is present, the solidification path departs from the tie-line on a length scale associated with solute diffusion as it approaches the cotectic line. Solute diffusion occurs on this scale to ensure that no supersaturation with respect to the second solidifying component occurs. The influence of solute diffusion is illustrated in figure 4, which shows solidification paths for different values of $\delta_B = \delta_C$. Increasing the solute diffusivities (decreasing δ_i) leads to a significant departure of the solidification path from the tie-line along the liquidus

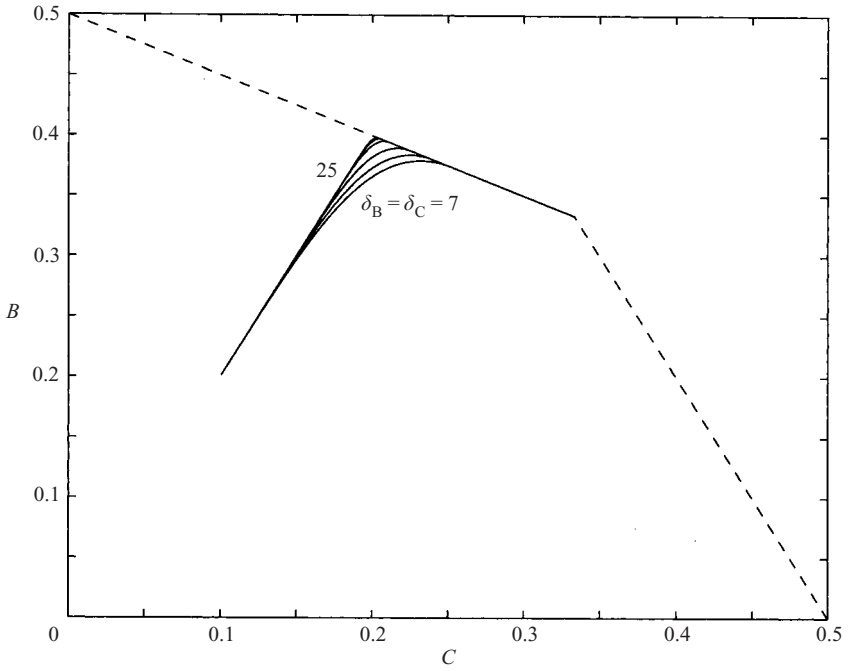

FIGURE 4. Solidification paths in the B–C plane for the parameter values in case (a) of table 1 when $\delta_B = \delta_C$ take the values 7, 8, 10, 15, 20 and 25. As the solutal diffusion is reduced the solidification path approaches the tie-line corresponding to the case of zero solutal diffusion. Note that $\delta_B = \delta_C = 25$ corresponds to a ratio $D_B/\kappa = D_C/\kappa \approx 10^{-3}$.

surface as the cotectic line is approached; physically, this corresponds to a thicker solute boundary layer above the mush–mush interface. The solidification paths for relatively small solutal diffusivities follow the tie-line nearly all the way along the liquidus surface before smoothly joining the cotectic line.

The temperature, liquid composition and solid fractions corresponding to case (a) in figure 3 are shown in figure 5. The material parameters used in these calculations are listed in table 1. In these plots the dashed lines indicate the three interface positions λ_P, λ_S and λ_E so that four layers (from the top, liquid layer, primary mushy layer, secondary mushy layer, eutectic solid layer) are shown. We observe that the liquid compositions are uniform in the liquid layer except within a narrow solutal boundary layer above the liquid–primary mush interface. Both B and C increase with depth through the primary mushy layer, as the A phase is preferentially incorporated into the solid, except in a boundary layer near the mush–mush interface where the trend in B reverses to accommodate the marginal equilibrium condition. In the secondary mushy layer B decreases with depth and C increases with depth to the eutectic composition as required by solidification down the cotectic curve. The primary mushy layer is characterized by a solid phase composed of solid A only. In the secondary mushy layer the solid is composed of solid A and a small amount of solid B as indicated. The eutectic solid is composed of A, B and C solid with proportions as shown.

The temperature, liquid compositions and solid fractions are qualitatively similar for the other solidification paths shown in figure 3. They differ quantitatively in the thickness of each layer (see figure 2) and the maximum solid fraction attained in each

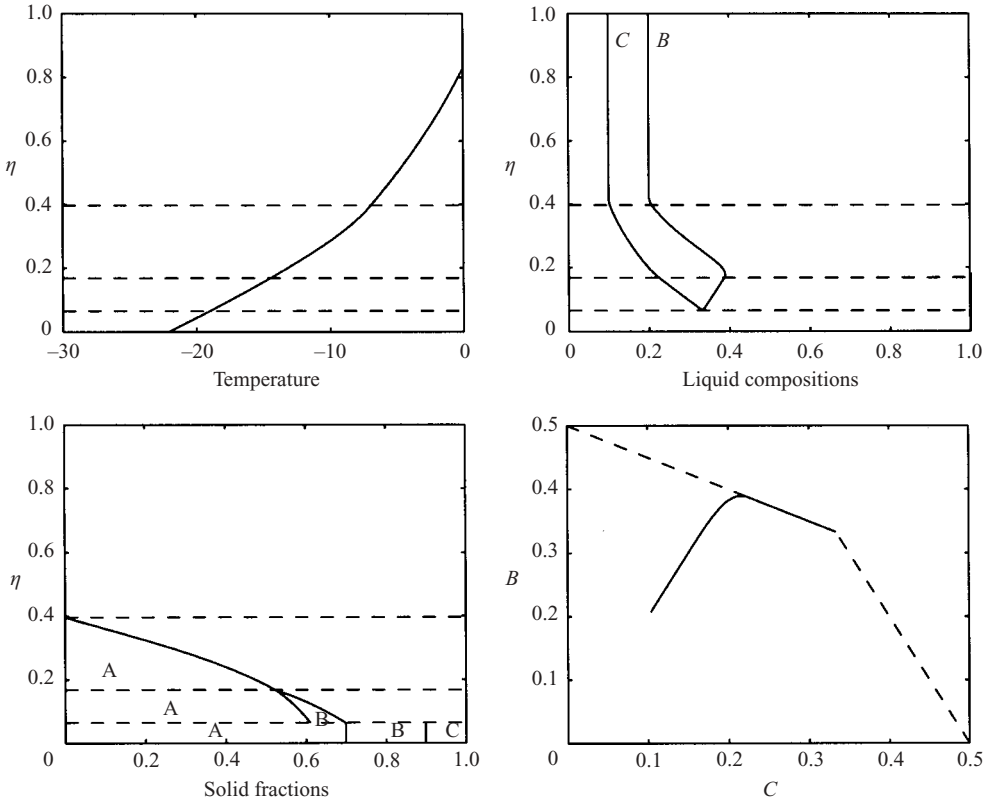

FIGURE 5. The solution profiles and solidification path for $B_\infty = 0.2$ and $C_\infty = 0.1$ (case a).

layer (see figure 6). Figure 6 indicates that the solid fraction values at the bottom of each mushy layer depend weakly on the thermal control parameters and depend strongly on the far-field compositions. In figure 6(c) varying B_∞ corresponds to a slice through (c), (a) and (d) in figure 3. As B_∞ increases, the primary layer thins and correspondingly the maximum-fraction solid A in the primary layer decreases. This can be understood by recognizing that, as B_∞ increases with C_∞ fixed, the value of A_∞ must decrease and therefore the formation of solid A in both layers must decrease. Physically, mass conservation dictates that an increase of one component A, B or C in the liquid is accompanied by an increase in the amount of the resulting solid phase. In figure 6(d) varying C_∞ corresponds to a slice through (b), (a) and (e) in figure 3. Note that for small values of C_∞ the liquid composition C cannot reach the (relatively large) eutectic composition C_E at the bottom of the secondary mushy layer until a significant proportion of A and B has been removed from the liquid and the solid fraction ($\phi_A^E + \phi_B^E$) is near unity. The general result that the solid fraction values appear to be nearly independent of the thermal controls may at first seem counterintuitive but it illustrates the importance of compositional effects in alloy systems such as the one considered here.

The analytical solution with zero solute diffusion and zero latent heat ($\gamma \to 0$ with γS_0 fixed and $\delta_B = \delta_C = \infty$) described in the previous section gives qualitatively similar results. We have examined the full solution in this limit in order to compare it with the analytical solution. Figure 7 shows the λ values for these two solution

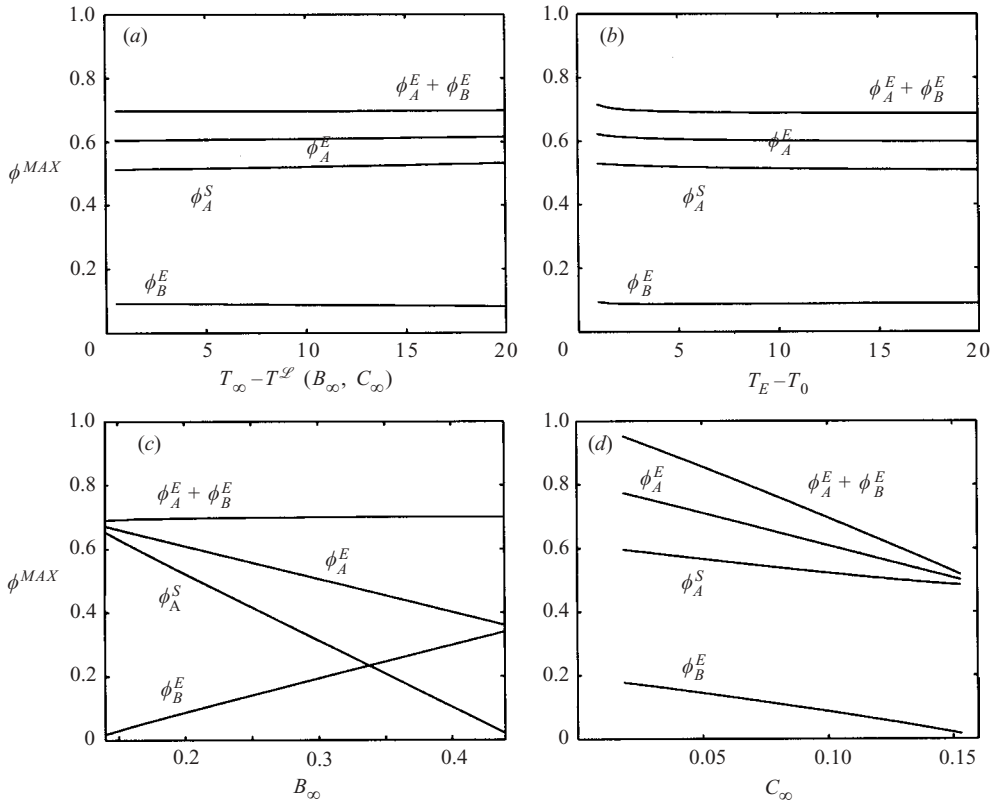

FIGURE 6. The solid fraction values at the bottom of the primary mushy layer (ϕ_A^S) and at the bottom of the secondary mushy layer (ϕ_B^E, ϕ_B^E and $\phi_A^E + \phi_B^E$) as the control parameters vary.

methods as the control parameters vary. In this figure the dashed curves indicate the analytical solution while the solid curves indicate the numerical solution calculated for $\gamma = -0.00001$, $S_0 = 5400$ and $\delta_B = \delta_C = 10$. The solution to the full code for these values compares favourably with the analytical solution. Differences observable in this plot can be associated with the relatively small values of δ_B and δ_C and can be further reduced by increasing the value of $\delta_B = \delta_C$ as shown in the data given in table 2.

In table 1, we show computations using both the analytical model and the full numerical model from which we can compare calculated λ values with those of experiments 6 and 7 reported by Aitta *et al.* Table 1 shows the parameter values used for these two comparisons (note that the analytical solution uses $\gamma = 0$, $S_0 = \infty$ and $\delta_B = \delta_C = \infty$, which are not physically realistic values for this system but still give correct order of magnitude estimates). We remark here that in the experimental results of Aitta *et al.* the solidification paths descend along the liquidus surface of the A corner (pure water). In experiment 6, secondary solidification occurs along the H_2O–$NaNO_3$ cotectic line and we correspondingly associate component B with $NaNO_3$. In experiment 7, secondary solidification occurs along the H_2O–KNO_3 cotectic line and we correspondingly associate component B with KNO_3. For both experiments 6 and 7 the model predictions for the interface positions (λ values) compare qualitatively well with the experimental results. Quantitatively, the primary

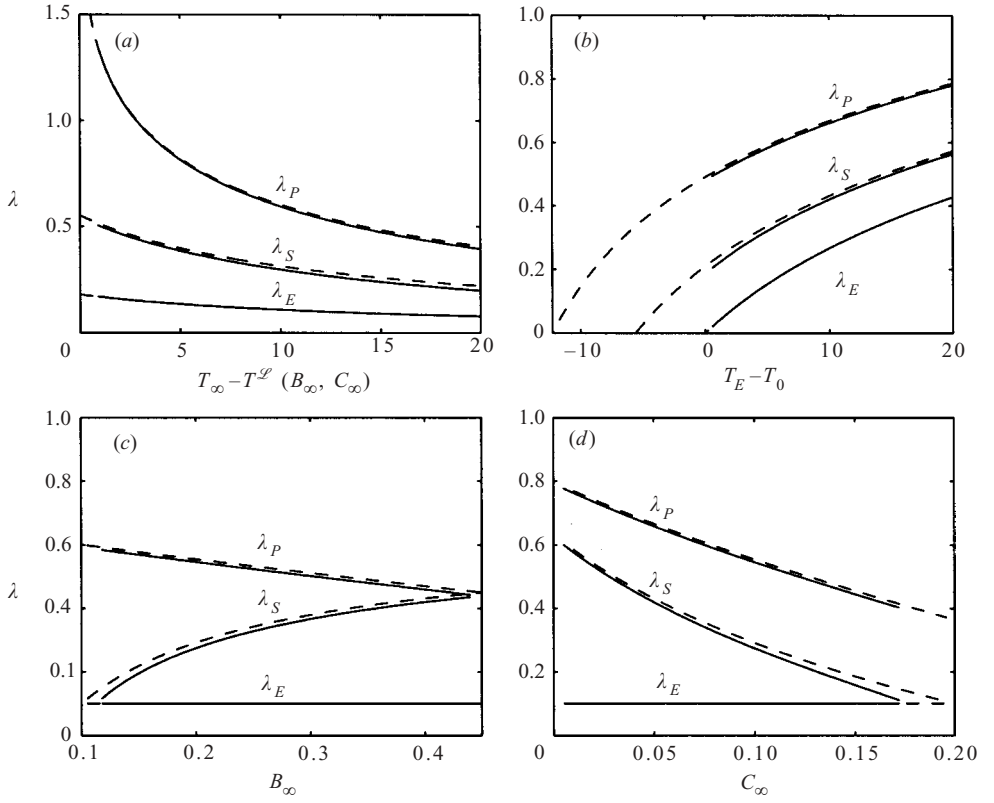

FIGURE 7. The λ values from equations (5.6) (dashed curves) and the numerical predictions of the full model with $\delta_B = \delta_C = 10$, $S_0 = 5400.0$ and $\gamma = -0.00001$ (solid curves) as a function of the control parameters. The slight differences between the solid and dashed curves can be eliminated by considering larger values of δ_B and δ_C (see table 2). Note that the analytical solution may be applied for base temperatures above the eutectic temperature so values of $T_E - T_0$ are extended accordingly.

(*a*)	Case	10	25	40	∞
	λ_P	0.5465	0.5541	0.5550	0.5555
	λ_S	0.2749	0.2894	0.2910	0.2921
	λ_E	0.1011	0.1011	0.1011	0.1011

TABLE 2. Numerical calculations for $\delta_B = \delta_C = 10, 25, 40$, $S_0 = 5400$ and $\gamma = -0.00001$ and also the results of the analytical solution ($\delta_B = \delta_C \to \infty$, $S_0 \to \infty$ and $\gamma \to 0$ with γS_0 fixed) corresponding to case (*a*). In the numerical solutions, convergence was achieved to four decimal places with respect to both the iteration procedure used to solve the differential equations and the spatial discretization.

mush interface position λ_P seems to be more accurately predicted than the other interface positions λ_S and λ_E, while that for the secondary mushy layer thickness $\lambda_S - \lambda_E$ (given by 0.029 for experiment 6 and 0.078 for experiment 7) are in slightly better agreement with the experimental values (0.045 for experiment 6 and 0.092 for experiment 7).

Discrepancies in the predicted values of λ_S and λ_E may be related to the significant nucleation delay reported by Aitta *et al.* for the cotectic and eutectic interfaces in their experiments. In particular, for their experiment 7, they report a 3–5 hour delay in nucleation of the eutectic solid. Once this growth began, it followed a linear scaling in time, suggestive of kinetically controlled growth, up to about 10 hours at which point the growth became diffusion-controlled, where $h_E \sim \sqrt{t}$. At early times ($t < 10$ h) they indicate that there was up to 10°C supercooling in the lower portion of the primary mushy layer and in the secondary mushy layer. For longer times ($t > 10$ h) there was up to 5°C supercooling, still in the secondary layer. We note that a 10°C change in the undercooling is approximately enough to cause the differences in λ values between experiment and theory based on the data in figure 2(*b*). That is, if an additional 10°C of undercooling was required to grow eutectic solid (i.e. T_E was 10°C lower) the predicted λ values would be smaller by approximately 0.1, which is the size of the discrepancy. Whether or not there are other factors contributing to these differences, it is clear that, at least initially, there are considerable non-diffusive and non-equilibrium effects present in the experiments, especially with respect to the lower portions of the mushy layers.

Finally, we note that Aitta *et al.* measured the λ_S interface position by locating the limit point in the B solute profile (this interface position could not be visually observed). Our theory suggests that the actual mush–mush interface is slightly below this limit point and so the experimentally reported interface position may be higher than the actual value, albeit by a small amount that is on the order of a solute boundary layer thickness.

7. Discussion of convective scenarios

Convection in a single mushy layer such as occurs during binary alloy solidification is known to have important effects on the dynamics of the evolving mushy layer and resultant microstructure in the solid (e.g. chimney formation and 'freckle' defects). Numerical simulations and experimental results have shown convection to be important in multicomponent alloys as well (e.g. Schneider *et al.* 1997; Krane *et al.* 1997, 1998; Felicelli *et al.* 1997, 1998; Beckermann, Gu & Boettinger 2000).

The double mushy layer geometry in the ternary alloy system gives rise to convective scenarios that are not present during binary alloy solidification. Aitta *et al.* (2001*b*) mapped out such convective scenarios for a simple ternary alloy system by identifying regimes in the ternary phase diagram and associated experimental growth configurations in which compositional convection was expected. In particular, for the fixed growth condition of cooling from below they identified cases in which compositional convection was expected in (i) neither mushy layer, (ii) only the primary mushy layer or (iii) both mushy layers. The conclusions are reversed when the cooling occurs from above. Their discussion applied to a situation in which the density depends in a symmetric way on the solute components B and C (see the next paragraph). We describe below a simple but more general density function which introduces a fourth basic compositional convection scenario. For clarity we include the scenarios previously addressed by Aitta *et al.* along with the additional case here.

Figure 8, which is an extension of figure 3 in Aitta *et al.* (2001*b*), shows a plan view sketch of the ternary phase diagram and indicates different regimes in which compositional convection can be predicted. The interior solid lines represent the cotectic boundaries. The long-dashed lines separate different regions of interest belonging to each of the three liquidus surfaces. The short-dashed lines are lines of

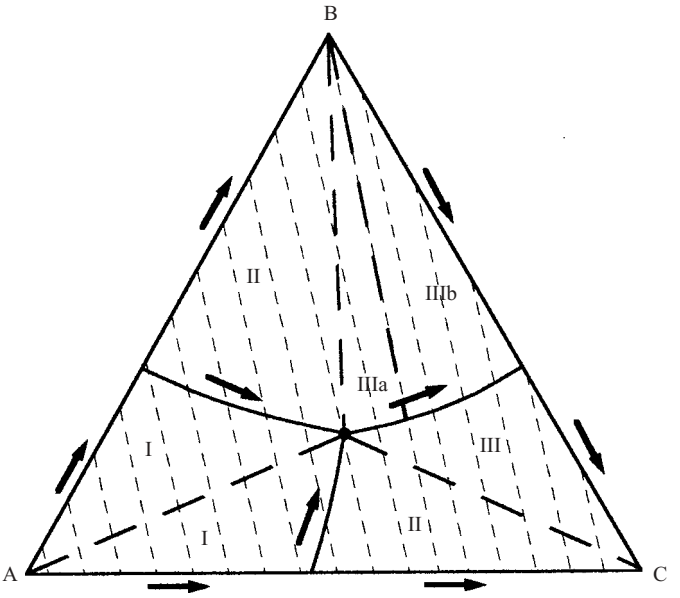

Solidification regime	Crystallized component	Fluid released	Compositional convection	
			Cooled below	Cooled above
I	A	heavy	no	yes
AB or AC cotectic	A + B or A + C	heavy	no	yes
II	B or C	light	yes	no
AB or AC cotectic	A + B or A + C	heavy	no	yes
III or IIIa	C or B	light	yes	no
BCcotectic	B + C	light	yes	no
IIIb	B	heavy	no	yes
BC cotectic	B + C	light	yes	no

FIGURE 8. Extension of Aitta *et al.* (2001*b*), figure 3 showing different regimes in the ternary phase diagram and whether or not compositional convection is expected. The interior solid curves correspond to the cotectic curves, the long-dashed lines indicate regions of interest in the diagram and the short-dashed curves are lines of constant density. Arrows indicate the direction along the boundary in which the density increases. These results include those of Aitta *et al.* but treat a more general density function that allows for the fourth convective scenario shown here.

constant density corresponding to the linear density function $\rho = \rho_0(1 + r_B B + r_C C)$ with $r_C > r_B > 0$. Here component A is the lightest and component C is the heaviest. Arrows show the direction along each boundary in which the density increases. For simplicity here we show only the case in which the thermal expansion coefficient is zero. We note that owing to the coupling between the temperature and composition through the phase diagram along any liquidus surface, for example, a general density function $\rho = \rho(T, B, C)$ can be expressed as a function of B and C alone. In the case of linear liquidus and density relations, the effective solutal expansion coefficients $\partial\rho(B, C)/\partial B = r_B^*$ and $\partial\rho(B, C)/\partial C = r_C^*$ are constants but depend on the particular liquidus surface under consideration. The effect of this in terms of figure 8 would be to reorient the density contours in each liquidus region with respect to the other two regions. For the purposes of the present discussion we shall focus on the density function defined above with zero thermal expansion and note that the qualitative predictions remain the same in either case. The discussion of Aitta *et al.* (2001*b*)

applied to the case in which $r_B = r_C$ so that the lines of constant density were parallel to the BC side of the ternary phase diagram. When $r_C > r_B$ there is a line of constant density that coincides with a tie-line from the B corner of the phase diagram. This line defines two regions (IIIa and IIIb in the figure) in which the convective scenarios differ. The density along tie-lines in region IIIa decreases (corresponding to a release of lighter fluid and hence compositional convection) while the density along the tie-lines in region IIIb increases (corresponding to a release of heavier fluid and hence no compositional convection). The details of these boundaries will change depending on the orientation of the cotectic boundaries with respect to the lines of constant density (in figure 8 most noticeably that of the AC cotectic), the inclusion of thermal expansion, and the incorporation of nonlinearity in the phase diagram or the density function. Independent of these details, however, four convective scenarios stand out.

Figure 8 shows that the ternary system can develop two mushy layers in which compositional convection may be possible in (i) neither mushy layer, (ii) the primary layer only, (iii) the secondary layer only, or (iv) both layers. In order to probe these cases more carefully, a Rayleigh number criterion for the onset of convection must be developed from these guidelines. The Rayleigh number measures the strength of compositional buoyancy relative to the resistance to flow due to the permeability of the mushy layer. Beckermann *et al.* (2000) have identified a global criterion for a critical Rayleigh number above which freckle formation is observed in experiments and numerical simulations for nickel-base superalloys. It is known that in the binary alloy case, convection can manifest itself in the form of a number of convective modes. These include steady modes, referred to as the boundary layer mode and the mushy layer mode (Worster 1992), and also oscillatory modes (Chen, Lu & Yang 1994; Anderson & Worster 1996). Our hope is that a detailed study of convection in ternary mushy layers may reveal the types of modes possible and the conditions for which they exist. For example, the resistance to flow in the secondary mushy layer, owing to the generally larger solid fraction than that of the primary mushy layer, may limit the influence of convection in this layer, as suggested by scaling analyses on binary alloy mushy layers by Krane & Incropera (1996). On the other hand, while the minimum solid fraction in the secondary mushy layer is bounded away from zero, numerical calculations for binary alloys suggest that channel formation may initiate somewhere in the interior of the mushy layer rather than at a mush–liquid interface (Schulze & Worster 1999). Beckermann *et al.* (2000) also argue that channel formation is probably initiated in the interior at a location where buoyancy forces are large enough and the permeability not too small. Whether such a balance can be found in the secondary mushy layer or if it necessarily occurs in the primary layer remains to be seen. Additional issues such as whether or not one layer may stabilize or destabilize the other are also unclear.

The above questions require analyses of a ternary alloy model that includes convective effects. The present description captures in a simple way four key convective scenarios associated with compositional buoyancy of two adjacent mushy layers and should represent a reasonable starting point for such an analysis.

8. Conclusions

We have developed a one-dimensional model for ternary alloy solidification that treats explicitly the double mushy layer geometry identified experimentally by Aitta *et al.* (2001*a*). The model includes thermal and solutal diffusion in conservation equations and incorporates a ternary phase diagram appropriate for their experimental

system. Interfacial conditions for the three boundaries (liquid–primary mush interface, primary–secondary mush interface, secondary mush–eutectic solid interface) are identified and described.

This model admits a similarity solution. An analytical solution is possible for the case in which solutal diffusion is absent and latent heat is zero. Numerical solutions are obtained for the general case. The numerical solution agrees well with the analytical solution in the appropriate parameter limit. Additionally, the full numerical model is in good agreement with a global model of Thompson *et al.* described in the Appendix.

The thickness of the primary mushy layer, secondary (or cotectic) mushy layer and eutectic layer depend strongly on the control parameters of the system. Variation of the far-field compositions leads to the possibility that the primary mushy layer is much thinner than the secondary mushy layer, as well as the opposite case where the primary mushy layer is much thicker than the secondary mushy layer. The solutions also show the temperature, solute and solid fraction distributions within each mushy layer.

Our analytical and numerical predictions capture qualitatively the features of the ternary mushy layer identified experimentally in Aitta *et al.* (2001*a*). Numerical predictions of the primary mushy layer interface position λ_P compare favourably with their experimental measurements. Predictions for the cotectic and eutectic interface positions do not agree as well, perhaps owing to the nucleation delay in the secondary and eutectic solidification reported experimentally.

The ternary mushy layer system is an exciting one from a fluid dynamics perspective. Scenarios exist in which one, both or neither of the two mushy layers may become convectively unstable. The hydrodynamic interactions between the two mushy layers are coupled to the dynamics of phase change. The wide variation in such quantities as the layer thicknesses and solid fraction distributions in the ternary mushy layer system will further influence this coupling. The fluid dynamical interactions with the phase change phenomena occurring in the ternary mushy layer system warrant further investigation.

The author would like to acknowledge support from the National Aeronautics and Space Administration Microgravity Science and Applications Program, the 3M Non-Tenured Faculty Award Program and also the Faculty Summer Research Support Program and the Junior Faculty Award Program in Social Sciences and Sciences of the College of Arts and Sciences at George Mason University. The author would also like to thank A. J. Kearsley, G. B. McFadden, T. P. Schulze and M. G. Worster for helpful discussions.

Appendix. A global conservation model for diffusion-controlled solidification of a ternary alloy

By Andrew F. Thompson, Herbert E. Huppert & M. Grae Worster
Institute of Theoretical Geophysics,
Department of Applied Mathematics and Theoretical Physics,
Centre for Mathematical Sciences, University of Cambridge,
Wilberforce Road, Cambridge, CB3 OWA, UK

Here we develop a simple model that relies only on global conservation of heat and solute (rather than local conservation as used above) to predict growth rates during diffusion-controlled solidification of a ternary alloy. Our analysis extends the global conservation model presented by Huppert & Worster (1985) for diffusion-controlled

growth of binary alloys, and later applied by Kerr *et al.* (1990*a*, *b*) to cases involving thermal convection. The global conservation model has three important simplifying assumptions that allow the mean solid fraction in each layer to be determined analytically, leaving the interface positions to be determined from conservation of heat.

First, in the absence of convection, the growth of a mushy layer is primarily controlled by thermal, rather than solutal, diffusion (Huppert & Worster 1985). Therefore we neglect solute diffusion in our model and note that the amount of solute in a given horizontal slice of the system then remains constant. This allows us to obtain the following exact integral relationships for the conservation of solute. In the primary mush

$$\int_{h_S}^{h_P} \left(1 - \phi_A^P\right) B \, \mathrm{d}z = B_\infty (h_P - h_S) \tag{A 1}$$

and in the cotectic mush

$$\int_{h_E}^{h_S} \left[\left(1 - \phi_A^S - \phi_B^S\right) B + \phi_B^S B_\beta\right] \, \mathrm{d}z = B_\infty (h_S - h_E), \tag{A 2}$$

$$\int_{h_E}^{h_S} \left(1 - \phi_A^S - \phi_B^S\right) C \, \mathrm{d}z = C_\infty (h_S - h_E), \tag{A 3}$$

where B_β represents a solid phase of pure component B and in the present context is equal to unity.

Again following the example of Huppert & Worster (1985), we select trial functions for the solid fractions such that the values of ϕ are an average over the thickness of a layer and therefore independent of z. We determine heat fluxes by assuming linear temperature profiles in each mushy layer and in the eutectic solid. A linear profile is consistent with the assumption of constant solid fraction when the Stefan number is large or when the time scale for the growth of the layer is short compared to the time scale for heat diffusion in the layer. Because of equilibrium thermodynamics and the assumption that the liquidus relationships are linear, concentration profiles in the residual liquid of the mushy layer are also linear with height.

We determine the temperature at the melt–mush interface T_P from the equation of the liquidus surface (2.1), and take the concentration at this interface to be equal to the uniform concentration of the melt. Since solute diffusion is neglected, we follow simple straight descent paths on the phase diagram and determine cotectic temperature and concentrations solely from the initial concentrations of the two solutes. Along the tie-line, $C = (C_\infty / B_\infty) B$. In addition the cotectic point is at the intersection of the tie-line and the cotectic curve. Thus equations (2.1) and (2.2) combine to give

$$T_S = \frac{T_E + m_B^{\mathscr{C}} (B_E - T_M / m_P)}{1 - m_B^{\mathscr{C}} / m_P}, \tag{A 4}$$

where $m_P = -m_B - (C_\infty / B_\infty) m_C$. The cotectic concentrations can then be determined from (2.2), so that temperature and liquid concentrations are known at each interface. We define linear temperature and concentration profiles in each layer by applying the interfacial values as boundary conditions.

Substituting the appropriate linear concentration profiles, such as

$$B = B_S + (B_\infty - B_S) \frac{z - h_S}{h_P - h_S} \tag{A 5}$$

in the primary mush and similar profiles in the cotectic mush, into equations (A 1)–(A 3), we obtain

$$\phi_A^P = \frac{B_S - B_\infty}{B_S + B_\infty}, \tag{A 6a}$$

$$\phi_B^S = \frac{B_\infty(C_S + C_E) - C_\infty(B_S + B_E)}{B_\beta(C_S + C_E)}, \tag{A 6b}$$

$$\phi_A^S = 1 - \phi_B^S - \frac{2C_\infty}{C_S + C_E}. \tag{A 6c}$$

Only the interface positions remain unknown, and they can be determined using the Stefan conditions (conservation of heat) at each interface. We seek a similarity solution, and define the interface positions as in equation (4.2). Substituting the temperature profile in the melt (4.3*a*) and the linear temperature profiles in the mushy layers and eutectic solid, we transform (3.3*a*), (3.5*a*) and (3.7*a*) to

$$2\lambda_P\kappa\left(\phi_A^P L_A\right) = \overline{k_P}\frac{(T_P - T_S)}{(\lambda_P - \lambda_S)} - 2k_l\lambda_P\frac{(T_\infty - T_P)}{F(\lambda_P)}, \tag{A 7}$$

$$2\lambda_S\kappa\left[\left(\phi_A^S - \phi_A^P\right)L_A + \phi_B^S L_B\right] = \overline{k_S}\frac{(T_S - T_E)}{(\lambda_S - \lambda_E)} - \overline{k_P}\frac{(T_P - T_S)}{(\lambda_P - \lambda_S)}, \tag{A 8}$$

$$2\lambda_E\kappa\left[\left(\phi_A^E - \phi_A^S\right)L_A + \left(\phi_B^E - \phi_B^S\right)L_B + \phi_C^E L_C\right] = \overline{k_E}\frac{(T_E - T_0)}{\lambda_E} - \overline{k_c}\frac{(T_S - T_E)}{(\lambda_S - \lambda_E)}. \tag{A 9}$$

Values for λ_P, λ_S and λ_E were determined by solving (A 7)–(A 9) simultaneously using a Newton–Raphson algorithm for a nonlinear system of equations taken from Press *et al.* (1992). The code can easily be extended to cases where $T_0 > T_E$ by modifying the equations above. In the case where $T_S > T_0 > T_E$, λ_P and λ_S are determined by solving (A 7) and (A 8) with T_E replaced by T_0 and λ_E set equal to zero. For $T_P > T_0 > T_S$, λ_P is determined from (A 7) with T_S replaced by T_B and λ_S set equal to zero.

Comparisons of the global conservation model with the local conservation model as the control parameters are varied individually are shown in figure 2. Agreement between the models is good except under the conditions of low superheat, when a weak logarithmic singularity develops in the local conservation model (Worster 1991). As the superheat approaches zero, there is no heat flux from the melt to limit growth of the primary mush, which has zero solid fraction at the melt–mush interface and hence no latent heat is released there.

Our global conservation model was also tested against the experiments conducted by Aitta *et al.* (2001*a*). A comparison of the parameters used in the local and global conservation models appears in table 3. The AHW/CRC data set, used in our global model, accounts slightly more for differences in material properties between the different components than the data set used in the local model.

Table 4 compares the similarity solutions measured in the experiments of Aitta *et al.* (2001*a*) to the global conservation model and, for experiments 6 and 7, the local conservation model also. The global conservation model was able to determine similarity solutions for all seven experiments although the initial concentrations of B_∞ needed to be adjusted slightly in experiments 1 and 4 (see table 4) to fall on the cotectic curve. For these two experiments only a cotectic mush will form. Comparison of the global conservation model with the experimental results shows good agreement for the primary and cotectic mushes in the cases when no eutectic solid forms. Agreement is not as good in experiment 4, which probably reflects the fact that the

	Local model	AHW/CRC
B_E^{AB}	0.10	0.091
C_E^{AB}	0.38	0.38
B_E	0.06	0.054
C_E	0.37	0.355
T_M [°C]	0	0
T_E^{AB} [°C]	−5.0	−2.84
T_E^{AC} [°C]	−16.4	−18.1
T_E [°C]	−19.0	−19.0
k_l/k_A	0.25	0.25
$k_l/k_{B,C}$	0.25	0.125
L_A/c_l [°C]	73.9	72.7
L_B/c_l [°C]	73.9	49.9
L_C/c_l [°C]	73.9	63.6

TABLE 3. Two sets of parameters for the ternary alloy, A–B–C = H_2O–KNO_3–$NaNO_3$, used by Aitta *et al.* (2001*a*). The first column are parameters used in the local conservation model developed in the main body of the paper, which uses the material properties of ice for the solid components. The second column is taken from Aitta *et al.* (2001*a*) and Lide (1997), and differentiates between the material properties of ice and the salts.

	Exp. 1		Exp. 2		Exp. 3		Exp. 4		Exp. 5	
B_∞	0.078		0.034		0.057		0.083		0.022	
C_∞	0.097		0.104		0.114		0.044		0.119	
T_∞ [°C]	20.0		20.0		20.0		20.0		20.0	
T_0 [°C]	−16.0		−15.0		−15.0		−16.0		−19.7	
	Exp.	Global	Exp.	Global	Exp.	Global	Exp.	Global	Exp.	Global
λ_P	–	–	0.365	0.349	0.299	0.306	–	–	0.475	0.469
λ_S	0.338	0.361	0.121	0.119	0.231	0.235	0.404	0.470	0.121	0.116
λ_E	–	–	–	–	–	–	–	–	–	0.0429

	Exp. 6				Exp. 7			
B_∞	0.012				0.035			
C_∞	0.146				0.152			
T_∞ [°C]	20.0				20.0			
T_0 [°C]	−27.7				−23.3			
	Exp.	Local	Global A	Global B	Exp.	Local	Global A	Global B
λ_P	0.570	0.581	0.602	0.663	0.496	0.463	0.480	0.527
λ_S	0.211	0.313	0.331	0.377	0.166	0.255	0.271	0.350
λ_E	0.166	0.284	0.293	0.363	0.0739	0.177	0.181	0.227

TABLE 4. Experimental control parameters and similarity solution results for the experiments conducted by Aitta *et al.* (2001*a*). Experiments 1–5 are compared to the global conservation model using the AHW/CRC parameters from table 3. B_∞ was changed from 8.0 to 7.8 in experiment 1 and from 8.4 to 8.3 in experiment 4 in order for it to fall on the cotectic curve. Experiments 6 and 7 are compared to the local conservation model (full version) developed in the main body of the paper and the global conservation model using parameters (Global A) and the AHW/CRC parameters (Global B) (table 3). The experimental values of λ were calculated from the a values in Aitta *et al.* (2001*a*) using their quoted value for the thermal diffusivity, $\kappa = 0.0011$ cm^2 s^{-1}.

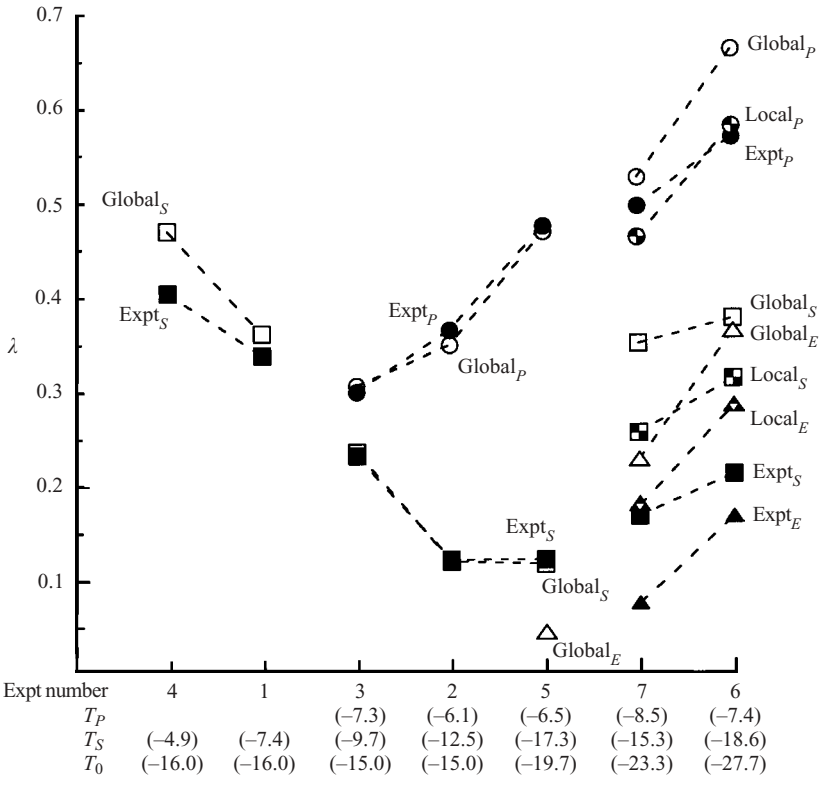

FIGURE 9. Comparison of the experimental values of λ with the results of the global and local conservation models. The horizontal axis indicates the experiment number as given in Aitta *et al.* (2001*a*) and table 4 as well as the temperatures at the melt–mush interface T_P, the primary–cotectic mush interface T_S and the base plate for each experiment T_0. The experiments have been divided into those that only formed a cotectic mush (4 and 1), those that formed both a primary and cotectic mush (3, 2 and 5) and those that formed both mushes and a eutectic solid (7 and 6). Within each group the experiments are listed according to their tie-lines on the phase diagram starting with the tie-line that intersects the H_2O–KNO_3 cotectic curve farthest away from the eutectic point and moving clockwise. Circles represent values of λ for the primary mush, while squares and triangles represent λ values for the cotectic mush and the eutectic solid respectively. Solid symbols stand for experimental values; open symbols correspond to the global conservation model and mixed symbols correspond to the local conservation model. The lines here only indicate groupings, and do not represent any interpolation between the experiments. Agreement between the experiments and the global conservation model for primary and cotectic mush growth rates is generally good in experiments 1–5. In experiments 6 and 7 agreement between the growth rates of the cotectic mush and the eutectic solid is not as good, probably because of a long nucleation delay in the formation of the eutectic solid.

initial conditions caused it to intersect the cotectic curve far from the eutectic point where there were less data available and where the assumption of linear liquidus relationships may not be as valid. Figure 9 shows a graphical representation of the information in table 4 for easier comparison of the results.

Agreement between the local and global models is also good for experiments 6 and 7 using the same parameters. Both models show reasonable agreement with the growth of the primary mush in the experiments, although the agreement with the

other two layers is not as good. This is probably due to nucleation delay, reported by Aitta *et al.* (2001*a*) to be on the order of hours for the eutectic layer.

The assumption of constant solid fraction implies that the latent heat is all released at the melt–mush interface (Kerr *et al.* 1990*a*). In fact, latent heat is released throughout the layer and since not all the heat is conducted away over the entire height, this assumption underestimates the rate of growth. Kerr *et al.* (1990*a*) also report that a second consequence of this assumption is that the effective conductivity of the layer is overestimated when the conductivities of the solid phases are greater than that of the liquid. Finally, contraction and expansion upon solidification have been ignored here even though the density of the salts is about twice that of the liquid. Neglecting this effect leads to an overestimation of the growth rates. This may also explain why agreement between the experiments and the model is weaker in cases where a eutectic solid forms, since there are relatively small quantities of solid salt in the mushy layers.

In conclusion, while both models suffer difficulties in modelling the growth of the eutectic solid for reasons discussed in the previous paragraph, the global conservation model provides results that are accurate to within 10% of the results of the local conservation model, and also gives reasonable agreement with experimental results.

REFERENCES

Aitta, A., Huppert, H. E. & Worster, M. G. 2001*a* Diffusion-controlled solidification of a ternary melt from a cooled boundary. *J. Fluid Mech.* **432**, 201–217.

Aitta, A., Huppert, H. E. & Worster, M. G. 2001*b* Solidification in ternary systems. In *Interactive Dynamics of Convection and Solidification* (ed. P. Ehrhard, D. S. Riley & P. H. Steen), pp. 113–122. Kluwer.

Anderson, D. M. & Worster, M. G. 1996 A new oscillatory instability in a mushy layer during the solidification of binary alloys. *J. Fluid Mech.* **307**, 245–267.

Beckermann, C., Gu, J. P. & Boettinger, W. J. 2000 Development of a freckle predictor via Rayleigh number method for single-crystal nickel-base superalloy castings. *Metall. Mater. Trans.* A **31**, 2545–2557.

Boettinger, W. J., Kattner, U. R., Coriell, S. R., Chang, Y. A. & Mueller, B. A. 1995 Development of multicomponent solidification micromodels using a thermodynamic phase diagram data base. In *Modelling of Casting, Welding and Advanced Solidification Process VII* (ed. M. Cross and J. Campbell), pp. 649–656. Warrendale, PA.

Chiareli, A. O. P. & Worster, M. G. 1992 On measurement and prediction of the solid fraction within mushy layers *J. Cryst. Growth* **125**, 487–494.

Chen, F., Lu, J. W. & Yang, T. L. 1994 Convective instability in ammonium chloride solution directionally solidified from below. *J. Fluid Mech.* **276**, 163–187.

Davis, S. H. 2001 *Theory of Solidification.* Cambridge University Press.

Felicelli, S. D., Poirier, D. R. & Heinrich, J. C. 1997 Macrosegregation patterns in multicomponent Ni–base alloys. *J. Cryst. Growth* **177**, 145–161.

Felicelli, S. D., Poirier, D. R. & Heinrich, J. C. 1998 Modelling freckle formation in three dimensions during solidification of multicomponent alloys. *Metall. Mater. Trans.* B **29**, 847–855.

Gu, J. P., Beckermann, C. & Giamei, A. F. 1997 Motion and remelting of dendrite fragments during directional solidification of a nickel–base superally. *Metall. Mater. Trans.* A **28**, 1533–1542.

Huppert, H. E. & Worster, M. G. 1985 Dynamic solidification of a binary melt. *Nature* **314**, 703–707.

Kerr, R. C., Woods, A. W., Worster, M. G. & Huppert, H. E. 1990*a* Solidification of an alloy cooled from above. Part 1. Equilibrium growth. *J. Fluid Mech.* **216**, 323–342.

Kerr, R. C., Woods, A. W., Worster, M. G. & Huppert, H. E. 1990*b* Solidification of an alloy cooled from above. Part 2. Non-equilibrium interfacial kinetics. *J. Fluid Mech.* **217**, 331–348.

Krane, M. J. M. & Incropera, F. P. 1996 A scaling analysis of the unidirectional solidification of a binary alloy. *Intl J. Heat Mass Transfer* **39**, 3567–3579.

Krane, M. J. M. & Incropera, F. P. 1997 Solidification of ternary metal alloys–II. Prediction of convective phenomena and solidification behavior of Pb–Sb–Sn alloys. *Intl J. Heat Mass Transfer* **40**, 3837–3847.

Krane, M. J. M., Incropera, F. P. & Gaskell, D. R. 1997 Solidification of ternary metal alloys–I. Model development. *Intl J. Heat Mass Transfer* **40**, 3827–3835.

Krane, M. J. M., Incropera, F. P. & Gaskell, D. R. 1998 Solidification of a ternary metal alloy: A comparison of experimental measurements and model predictions in a Pb–Sb–Sn system. *Metall. Mater. Trans.* A **29**, 843–853.

Lide, D. R. 1997 *CRC Handbook of Chemistry and Physics*, 78th Edn. CRC Press.

Press, W. H., Teukolsky, S. A., Vetterling, W. T. & Flannery B. P. 1992 *Numerical Recipes in Fortran 77: The Art of Scientific Computing*, 2nd Edn. Cambridge University Press.

Schneider, M. C. & Beckermann, C. 1995 A numerical study of the combined effects of microsegregation, mushy zone permeability and flow, caused by volume contraction and thermosolutal convection, on macrosegregation and eutectic formation in binary alloy solidification. *Intl J. Heat Mass Transfer* **38**, 3455–3473.

Schneider M. C., Gu, J. P., Beckermann, C., Boettinger, W. J. & Kattner, U. R. 1997 Modelling of micro- and macrosegregation and freckle formation in single-crystal nickel-base superalloy directional solidification. *Metall. Mater. Trans.* A **28**, 1517–1531.

Schulze, T. P. & Worster, M. G. 1999 Weak convection, liquid inclusions and the formation of chimneys in mushy layers. *J. Fluid Mech.* **388**, 197–215.

Smallman, R. E. 1985 *Modern Physical Metallurgy*. Butterworths.

Voller, V. R. 1997 A similarity solution for the solidification of a multicomponent alloy. *Intl J. Heat Mass Transfer* **40**, 2869–2877.

Worster, M. G. 1986 Solidification of an alloy from a cooled boundary. *J. Fluid Mech.* **167**, 481–501.

Worster, M. G. 1991 Natural convection in a mushy layer. *J. Fluid Mech.* **224**, 335–359.

Worster, M. G. 1992 The dynamics of mushy layers. In *Interactive Dynamics of Convection and Solidification* (ed. S. H. Davis, H. E. Huppert, U. Müller & M. G. Worster), pp. 113–138. Kluwer.

Worster, M. G. 1997 Convection in mushy layers. *Annu. Rev. Fluid Mech.* **29**, 91–122.

Worster, M. G. 2000 Solidification of Fluids. In *Perspectives in Fluid Dynamics* (ed. G. K. Batchelor, H. K. Moffatt & M. G. Worster), pp. 393–446. Cambridge University Press.

Worster, M. G. 2002 Interfaces on all scales during solidification and melting. In *Interfaces for the Twenty-First Century* (ed. M. K. Smith, M. J. Miksis, G. B. McFadden, G. P. Neitzel & D. R. Canright), pp. 187–201. Imperial College Press.